# Climate feedbacks derived from spatial gradients in recent climatology

Philip Goodwin<sup>1</sup>, Richard Guy Williams<sup>2</sup>, Paulo Ceppi<sup>3</sup>, and B. B. Cael<sup>4</sup>

December 23, 2024

#### Abstract

Climate feedbacks, including Planck, surface albedo, water vapor-lapse rate (WVLR) and cloud feedbacks, determine how much surface temperatures will eventually warm to balance anthropogenic radiative forcing. Climate feedbacks remain difficult to constrain directly from temporal variation in observed surface warming and radiation budgets due to the short historical record and low signal-to-noise ratio, with only order 1{degree sign}C historic rise in surface temperatures and high uncertainty in aerosol radiative forcing. This study presents a new method to analyze climate feedbacks from observations by empirically fitting simplified reduced-physics relations for outgoing radiation at the top of the atmosphere (TOA) to observed spatial variation in climate properties and radiation budgets. Spatial variations in TOA outgoing radiation are dominated by the dependence on surface temperature: around 85% of the spatial variation in clear sky albedo, and 78% of spatial variation in clear sky TOA outgoing longwave radiation, is functionally explained by variation in surface temperatures. These simplified and observationally constrained relations are then differentiated with respect to spatial contrasts in surface temperature to reveal the Planck, surface albedo ( $\lambda$ -abedo) and WVLR ( $\lambda$ -WVLR) climate feedbacks spatially for both clear sky and all sky conditions. The resulting global all sky climate feedback values are  $\lambda$ -WVLR=1.30 (1.20 to 1.40 at 66%) Wm-2K-1, and  $\lambda$ -abedo=0.60 (0.53 to 0.66) Wm-2 for the 2003-2023 period reducing to 0.32 (0.28 to 0.35) Wm-2K-1 under 4{degree sign}C warming after cryosphere retreat. Our findings agree well with complex Earth system model evaluations based on temporal climate perturbations, and our approach is complementary.

# Hosted file

GWCC\_JGRAtmos\_resubmission.docx available at https://authorea.com/users/543395/articles/1253632-climate-feedbacks-derived-from-spatial-gradients-in-recent-climatology

#### Hosted file

GWCC\_JGRAtmos\_SuppInfo\_revision.docx available at https://authorea.com/users/543395/articles/1253632-climate-feedbacks-derived-from-spatial-gradients-in-recent-climatology

<sup>&</sup>lt;sup>1</sup>University of Southampton

<sup>&</sup>lt;sup>2</sup>University of Liverpool

<sup>&</sup>lt;sup>3</sup>Imperial College London

<sup>&</sup>lt;sup>4</sup>National Oceanography Centre

2

# Climate feedbacks derived from spatial gradients in recent climatology

- 3 P. Goodwin<sup>1</sup>, R. G. Williams<sup>2</sup>, P. Ceppi<sup>3</sup>, and B. B. Cael<sup>4,5</sup>
- <sup>1</sup>School of Ocean and Earth Science, University of Southampton, SO14 3ZH, UK.
- <sup>2</sup>Department of Earth, Ocean and Ecological Sciences, School of Environmental Sciences,
- 6 University of Liverpool, Liverpool, L69 3GP UK.
- <sup>3</sup>Department of Physics, Imperial College London, London, SW7 2AZ, UK.
- <sup>4</sup>Ocean Biogeosciences, National Oceanography Centre, European Way, Southampton, SO14
- 9 3ZH, UK.
- <sup>5</sup>Department of the Geophysical Sciences, University of Chicago, IL, USA
- 11 Corresponding author: Philip Goodwin (p.a.goodwin@soton.ac.uk)

# **Key Points:**

- Earth's radiation budget is empirically related to surface and atmospheric properties in recent climatology using simplified theory
- Spatial variations in outgoing radiation are dominated by their dependence on surface temperature
- Climate feedbacks are evaluated spatially by differentiating the simplified theory with respect to surface temperature

18 19

12

13

14

15

16

# **Abstract**

Climate feedbacks, including Planck, surface albedo, water vapor-lapse rate (WVLR) and cloud feedbacks, determine how much surface temperatures will eventually warm to balance anthropogenic radiative forcing. Climate feedbacks remain difficult to constrain directly from temporal variation in observed surface warming and radiation budgets due to the short historical record and low signal-to-noise ratio, with only order 1°C historic rise in surface temperatures and high uncertainty in aerosol radiative forcing. This study presents a new method to analyze climate feedbacks from observations by empirically fitting simplified reduced-physics relations for outgoing radiation at the top of the atmosphere (TOA) to observed spatial variation in climate properties and radiation budgets. Spatial variations in TOA outgoing radiation are dominated by the dependence on surface temperature: around 85% of the spatial variation in clear sky albedo, and 78% of spatial variation in clear sky TOA outgoing longwave radiation, is functionally explained by variation in surface temperatures. These simplified and observationally constrained relations are then differentiated with respect to spatial contrasts in surface temperature to reveal the Planck, surface albedo ( $\lambda_{ahedo}$ ) and WVLR  $(\lambda_{WVLR})$  climate feedbacks spatially for both clear sky and all sky conditions. The resulting global all sky climate feedback values are  $\lambda_{WVLR}$ =1.30 (1.20 to 1.40 at 66%) Wm<sup>-2</sup>K<sup>-1</sup>, and  $\lambda_{abedo}$ =0.60 (0.53 to 0.66) Wm<sup>-2</sup> for the 2003-2023 period reducing to 0.32 (0.28 to 0.35) Wm<sup>-2</sup>K<sup>-1</sup> under 4°C warming after cryosphere retreat. Our findings agree well with complex Earth system model evaluations based on temporal climate perturbations, and our approach is complementary.

# **Plain Language Summary**

The climate feedback measures how much Earth's surface temperatures will change in response to climate forcing from rising greenhouse gas concentrations. However, our observed record of surface temperature changes over time in response to rising greenhouse gas concentrations in the past is not long enough to accurately determine Earth's climate feedback for the future. In part, this limitation is because recent anthropogenic warming has only reached around 1 degree Celsius of temperature change globally so far. Here, we take an alternative approach: instead of considering how Earth's surface temperatures have changed over time we consider how Earth's surface temperatures change from the cold polar regions to the warm tropics which provides a much larger temperature change of around 80 degrees Celsius. By accounting for the different physical processes that affect Earth's surface temperature spatially, we are able to provide an estimate of the climate feedback in response to a climate forcing from greenhouse gas concentrations. Our spatial-change estimates of climate feedback are independent of the existing temporal-change estimates, but are in good agreement with current estimates of climate feedback.

#### 1. Introduction

An imbalance in Earth's energy budget at the top of the atmosphere is eventually restored through climate feedback processes, whereby an increase in surface temperatures leads to an increase in outgoing radiation at the top of the atmosphere (TOA). The total climate feedback from all processes,  $\lambda_{total}$  in Wm<sup>-2</sup>K<sup>-1</sup>, is defined as minus the partial derivative of outgoing radiation at the top of the atmosphere,  $R_{out}$  in Wm<sup>-2</sup>K<sup>-1</sup>, with respect to surface temperature,  $T_S$  in K,

$$\lambda_{total} = -\frac{\partial R_{out}}{\partial T_S} \qquad . \tag{1}$$

 $\lambda_{total}$  for the present day Earth system is an important quantity in global climate science, since it is inversely linked to the Equilibrium Climate Sensitivity, ECS $\sim 1/\lambda_{total}$ , and so determines the future surface warming response to some specified anthropogenic forcing. This total climate feedback may be decomposed into individual climate feedbacks from different processes,  $\lambda_{total} = \sum \lambda_X$ , where the feedback from process X is,

$$\lambda_X = -\frac{\partial R_{out}}{\partial T_S} \Big|_{\delta X} = -\frac{\partial [S_{out} + L_{out}]}{\partial T_S} \Big|_{\delta X} = -\frac{\partial [S_{out} + L_{out}]}{\partial X} \frac{\partial X}{\partial T_S} \quad , \tag{2}$$

where  $S_{out}$  is the outgoing shortwave radiation and  $L_{out}$  is the outgoing longwave radiation at the TOA. The different climate feedback processes,  $\lambda_X$ , include the Planck feedback, the water vapor-lapse rate (WVLR) feedback, the surface albedo feedback and cloud feedbacks; see Sherwood et al. (2020) for a comprehensive assessment.

Existing studies quantify climate feedbacks (either as the total feedback or the separate contributions from individual processes) through temporal changes in surface temperatures and Earth's energy budget at the top of the atmosphere using either observations, numerical simulations or paleoclimate archives (e.g. Sherwood et al., 2020). However, temporal observations have only a limited historic record, especially for the energy budget, and the observed anthropogenic warming signal of around 1K is relatively small in comparison to the interannual variability and the uncertainty of the radiative effects of aerosols (Sherwood et al., 2020).

Climate feedbacks are readily evaluated from numerical climate model simulations (e.g. Soden et al., 2008; Zelinka et al., 2020), which can use idealized forcing without aerosol contributions and simulate a longer time period than the historic record. While modern climate models include sophisticated representations of physical processes, the evaluated climate feedbacks do differ between different models (e.g. Zelinka et al., 2020), and so any single numerical model simulations may be biased relative to the real world. Also, if the goal is to evaluate the climate feedback contributions from different individual processes,  $\lambda_X$ , then the relatively large finite perturbations employed in numerical climate models lead to linear combination error in the individual feedbacks, such that  $\lambda_{total} \neq \sum \lambda_X$  (e.g. the rms difference between  $\lambda_{total}$  and  $\sum \lambda_X$  is 17.2 % for 27 CMIP6 models assessed by Zelinka et al., 2020, and 17.7 % for 28 CMIP5

models). Note that this nonlinear effect only impacts the values of  $\lambda_X$  for each process and does not impact the value of the total climate feedback,  $\lambda_{total}$ .

Consider an alternative approach based on the spatial variation in TOA outgoing radiation and surface temperature (Figure 1). Evaluated with 1° horizontal resolution during the 2003-2023 period, surface temperature correlates to TOA outgoing radiation and explains some 74 % of the variance in TOA outgoing radiation (Fig. 1), with a sensitivity of  $\frac{\delta R_{out}}{\delta T_S} \approx 1.28 \ \text{Wm}^{-2} \text{K}^{-1}$ . This crude observational estimate is consistent in magnitude to recent estimates of climate feedback (e.g.  $\lambda_{total} = -\partial R_{out}/\partial T_S = -1.30 \pm 0.44$  in Sherwood et al., 2020). However, it is not in general robust to assume that the value of  $\delta R_{out}/\delta T_S$  analyzed spatially and the value of  $\partial R_{out}/\partial T_S$  are similar: a significant part of the observed spatial variation in  $R_{out}$  may arise from factors that co-vary in space with  $T_S$  in recent climatology, but would not co-vary in time following a perturbation to the climate system.

Previous studies in the literature have successfully related TOA outgoing radiation to parameters describing atmospheric and surface properties, either empirically or theoretically (e.g. Raval and Ramanathan, 1989; Koll and Cronin, 2018; Schmidt et al., 2010; Ingram, 2010), and so have described combinations of processes and parameters that explain variation in  $R_{out}$ . However, in general these empirically fitted relations for  $R_{out}$  are not easily differentiable with respect to surface temperature so cannot then be used to diagnose the climate feedback, (1).

The goal of this study is to evaluate climate feedbacks from the Planck, WVLR and surface albedo feedback processes using observations of the *spatial* variation in TOA outgoing radiation, surface temperature and other properties of the Earth's surface and atmosphere (where these other properties preferably vary independently of surface temperature). *Spatial* variation in observed surface temperature is of order 80 K (Fig. 1), thus providing a better signal-to-noise ratio than the much smaller order 1K *temporal* variation in observed surface temperature. To evaluate climate feedbacks, we first empirically relate  $R_{out}$  to  $T_S$  and other atmospheric and surface properties using functional forms that are easily differentiable with respect to surface temperature. The analysis is conducted on a 1° by 1° spatial resolution using climatology for the 2003-2023 period, evaluating non-cloud feedbacks and for both clear skies conditions and all skies conditions assuming constant cloud amount and cloud properties. Additional climate feedbacks associated with changes in cloud amount or cloud properties are not considered.

Recent studies have estimated climate feedbacks from theory and/or spatial variation in climate properties (e.g. Feldl and Merlis, 2023; Kroll et al., 2023). Feldl and Merlis (2023) use theory and spatial variation in climate properties to calculate climate feedback, but crucially the theory in their method does not solve for the radiative properties of the system, and instead employs radiative kernels (e.g. Soden et al., 2008) evaluated from model output forced with finite perturbations. Therefore, the Feldl and Merlis (2023) method does not provide an assessment of climate feedback terms that is independent of the numerical climate models. Kroll et al. (2023) solves for a climate feedback term from first principles theoretically, and so

- does not require numerical model input, but solves for the longwave climate feedback under
- clear sky conditions only. The aim here is to solve for climate feedback terms involving Planck,
- 150 WVLR and surface albedo, each under both clear sky and all sky conditions, using theory applied
- to observational data for the climatological mean state. The climate feedbacks are solved
- independently of both numerical model output or time-varying climate signals.
- 153 Section 2 of this study derives and empirically fits new reduced physics, simplified relations
- describing variation in TOA outgoing radiation in terms of surface temperature and other
- surface and atmospheric properties. Section 3 then differentiates these simplified relations to
- evaluate the Planck, WVLR and surface albedo climate feedbacks under clear sky and all sky
- 157 conditions.

# 2. Simplified empirical relations for outgoing radiation at the TOA

159 160 161

# 2.1 A framework for TOA outgoing radiation, planetary emissivity and planetary albedo

- 162 A framework is adopted to derive the functional relationships where outgoing radiation under
- sky condition i (signifying either clear-sky, cloudy-sky or all-sky conditions) is related to the
- Stefan-Boltzman constant,  $\sigma$  in Wm<sup>-2</sup>K<sup>-4</sup>, surface temperature,  $T_S$ , and incident solar radiation
- via,  $R_{in}$ , in Wm<sup>-2</sup>, via,

166

$$R_{out,i}(x,y) = L_{out,i}(x,y) + S_{out,i}(x,y) = \varepsilon_i(x,y)\sigma T_S^4(x,y) + \alpha_i(x,y)R_{in}(x,y)$$
(3)

167 168 169

- where the planetary emissivity  $\varepsilon_i$  is defined by the outgoing longwave radiation at the top of
- the atmosphere as a fraction of the expected emitted radiation at the planet's surface for a
- 171 black body averaged over some time span,

172

173 
$$\varepsilon_i(x,y) = \int_t^{t+n\Delta t} \frac{L_{out,i}(x,y,t')}{\sigma T_S^4(x,y,t')} dt' / \int_t^{t+n\Delta t} dt' , \qquad (4a)$$

174175

- and the planetary albedo  $\alpha_i$  in eq. (3) is defined as the outgoing shortwave radiation at the top of the atmosphere as a fraction of incident solar radiation at the top of the atmosphere
- of the atmosphere as a fraction of incider averaged over some time span,

178179

$$\alpha_i(x,y) = \int_t^{t+n\Delta t} \frac{S_{out,i}(x,y,t')}{R_{in}(x,y,t')} dt' / \int_t^{t+n\Delta t} dt'$$
 (4b)

180 181

# 2.1.1 Planetary emissivity

- The definition of planetary emissivity adopted here,  $\varepsilon_i$  in eq. (4a), considers outgoing radiation
- measured at the top of the atmosphere and emitted radiation measured at the planet's
- surface. This planetary emissivity therefore accounts for both the direct emissivity effect of the
- surface material of the planet (where emitted radiation is less than  $\sigma T_S^4$ ) and the greenhouse
- effect of the atmosphere (where the atmosphere both absorbs and re-emits longwave radiation
- so that the outgoing longwave radiation at the top of the atmosphere is less than the upward
- longwave radiation at the planet's surface). Note that the Sherwood et al. (2020) climate

feedback review also utilizes the same planetary emissivity definition when analyzing the Planck feedback.

The climatological monthly mean clear sky planetary emissivity,  $\varepsilon_{ClearSky}(x,y)$ , for the period 2003-2023 varies spatially from 0.57 to 1.0 (Fig. 2, left hand column), with low values in tropical regions and high values near the poles. This range of values implies that atmospheric absorption and emission of radiation and surface emissivity properties reduce the top of the atmosphere outgoing longwave radiation, relative to the expected longwave blackbody radiation emitted by the Earth's surface, by up to 43 % under clear skies. In all sky conditions, monthly mean planetary emissivity,  $\varepsilon_{AllSky}$ , varies spatially from 0.39 to 1.0, such that in the presence of clouds outgoing longwave radiation at the top of the atmosphere is reduced by up to 61 % relative to the expected surface emission by a blackbody.

# 2.1.2 Planetary albedo

The definition of planetary albedo definition adopted here,  $\alpha_i$  in eq. (4b), considers incident and reflected radiation both measured at the top of the atmosphere. This planetary albedo definition therefore accounts for the shortwave radiation reflection both by the planet's surface and by atmospheric constituents in either clear sky, cloudy sky or all sky conditions. The monthly climatological planetary albedo varies spatially from <0.10 to 0.88 in clear sky conditions and 0.10 to 0.96 in all sky conditions (Fig. 3).

# 2.1.3 Differential forms for planetary emissivity and planetary albedo

From eq. (3) we can see that the TOA outgoing shortwave radiation is related to incoming solar radiation by  $S_{out,i}(x,y) = \alpha_i(x,y)R_{in}(x,y)$  and the TOA outgoing longwave radiation is related to the expected blackbody emission at the Earth's surface by  $L_{out,i}(x,y) = \varepsilon_i(x,y)\sigma T_S^4(x,y)$  under sky condition i. The values of planetary albedo and planetary emissivity vary spatially (Figs. 2, 3) and with surface temperature (Fig. 4). The goal is therefore to identify reduced physics simplified relations for  $\alpha_i$  and  $\varepsilon_i$  that are differentiable with respect to surface temperature to identify the Planck, WVLR and surface albedo climate feedbacks in clear sky and all sky conditions.

In order to be differentiable with respect to surface temperature to evaluate the climate feedback, the simplified relations that solve for TOA outgoing shortwave and longwave radiation, via solving for  $\alpha_i$  and  $\varepsilon_i$ , must only contain parameters that are relatively insensitive to perturbations in surface temperature. Consider two simplified functions where planetary emissivity is related to surface temperature and J other parameters describing the atmospheric and surface properties,

$$\varepsilon_i = f(T_S, x_1, x_2 \dots x_J) \tag{5a}$$

and planetary albedo is related to surface temperature and K other properties,

231 
$$\alpha_i = g(T_S, y_1, y_2 \dots y_K)$$
 (5b)

Ideally, we should like all other parameters to be orthogonal to  $T_S$  under climate perturbation 233 so that so that we are to differentiate these functions, f and g, with respect to surface 234

temperature without knowing the sensitivity of each separate parameter to  $T_S$ ,  $\frac{\partial X_j}{\partial T_S}$ . Given that 235

we may not be able to identify parameters that are perfectly orthogonal to  $T_S$  and still 236

accurately capture the variation in  $\varepsilon_i$  and  $\alpha_i$ , then we require: 237

238

$$|\frac{\partial \varepsilon_i}{\partial T_S}| \gg \left| \frac{\partial x_j}{\partial T_S} \frac{\partial \varepsilon_i}{\partial x_j} \right|$$
 (6a)

240

for each of the J parameters that are not  $T_S$  in the emissivity relation (5a) and 241

242 243

$$\left| \frac{\partial \alpha_i}{\partial T_S} \right| \gg \left| \frac{\partial y_k}{\partial T_S} \frac{\partial \alpha_i}{\partial y_k} \right| \tag{6b}$$

244

- for each of the K parameters that are not  $T_S$  in the albedo relation (5b). Therefore, here we 245 cannot use parameters such as total precipitable column water vapor or specific humidity, since 246 247 these parameters vary significantly over time with a surface temperature perturbation. For example, if  $x_j$  were precipitable water vapor column then after temperature increase  $x_j$  would 248
- also increase,  $\frac{\partial x_j}{\partial T_s} > 0$ , since warm air holds more water vapor. This increase in precipitable 249
- water vapor column then reduces planetary emissivity,  $\frac{\partial \varepsilon_i}{\partial x_i} < 0$ , from the greenhouse effect. 250
- Therefore the magnitude  $\left| \frac{\partial x_j}{\partial T_S} \frac{\partial \varepsilon_i}{\partial x_j} \right|$  could be considerable, and break condition (6a). However, 251
- instead we can use parameters such as surface relative humidity and the height of the 252
- tropopause (that are related to specific humidity and total precipitable water vapor content), 253
- since the changes in these quantities over time after temperature perturbation have a greater 254
- chance of satisfying condition (6a) and (6b). For example, if  $x_i$  were relative humidity then  $x_i$ 255
- would not likely change significantly with surface warming,  $\frac{\partial x_j}{\partial T_s} \sim 0$ , and so  $\left| \frac{\partial x_j}{\partial T_s} \frac{\partial \varepsilon_i}{\partial x_i} \right|$  would 256
- satisfy condition (6a). 257

258 259

260

# 2.1.4 Clear sky, cloudy sky and all sky conditions

- In clear sky conditions, the 2003-2023 annual-mean climatology evaluated planetary emissivity, 261
- $\varepsilon_{ClearSky}$ , is nearly linearly related to surface temperature (Fig. 4e):  $\frac{\delta \varepsilon_{ClearSky}}{\delta T_S} = -3.75 \text{ K}^{-1} \text{ with}$ 262
- R<sup>2</sup> of 0.96 (see Koll and Cronin, 2018). The 2003-2023 annual-mean climatology evaluated clear 263
- sky albedo,  $\alpha_{ClearSky}$  (Fig. 4f), shows a relationship to surface temperature with generally high 264
- albedo for annual-mean temperatures below 260 K and generally low albedo for annual-mean 265
- temperatures above 270 K. Since climate feedbacks are related to the partial derivative of 266
- outgoing radiation with respect to surface temperature (eqs. 1, 2), this study aims to identify 267
- the partial derivatives,  $\frac{\partial \varepsilon_{ClearSky}}{\partial T_S}$ ,  $\frac{\partial \varepsilon_{AllSky}}{\partial T_S}$ ,  $\frac{\partial \alpha_{ClearSky}}{\partial T_S}$  and  $\frac{\partial \alpha_{AllSky}}{\partial T_S}$  through observation-268

constrained functional relationships that are used to extract the impact of any factors that co-269 270 vary spatially with surface temperature in recent climatology (Fig. 4).

271

The planetary emissivity and albedo for the three different sky conditions, all sky, clear sky and 272 273 cloudy sky, are connected via,

274

$$\varepsilon_{AllSky}(x,y) = f_{CA}(x,y)\varepsilon_{CloudySky}(x,y) + [1 - f_{CA}(x,y)]\varepsilon_{ClearSky}(x,y)$$
 (7a)

276 and

277

$$\alpha_{AllSky}(x,y) = f_{CI}(x,y)\alpha_{CloudySky}(x,y) + [1 - f_{CI}(x,y)]\alpha_{ClearSky}(x,y)$$
 (7b)

- where  $f_{CA}$  is the cloud amount area fraction and  $f_{CI}$  is the cloud incident radiation fraction. 279
- 280 Note that when averaging over time the cloud incident radiation fraction may differ from the
- 281 cloud amount area fraction, and is calculated via

282

$$f_{CI}(x,y) = \frac{\sum f_{CA}(x,y,m)R_{in}(x,y,m)\Delta t_m}{\sum R_{in}(x,y,m)\Delta t_m}$$
(8)

284

283

285 where m is some time interval.

286 287

288

Section 2.1 considers the planetary emissivity and albedo in clear sky conditions, while section 2.2 explores the impact of clouds in modifying the planetary emissivity and albedo in all sky conditions.

289 290

# 2.2 TOA outgoing radiation in clear skies

291 292 293

# 2.2.1 Outgoing Shortwave radiation for Clear Sky

294 Simplified functional relationships are now assessed for clear sky surface albedo in terms of 295

surface temperature and other properties of the climate system. Here, we allow clear sky albedo to be a function of surface temperature  $T_s$ , whether the surface is land or ocean, k, and latitude  $\phi$ ,

297 298 299

296

$$\alpha_{ClearSky} \approx f(T_s, k, \phi)$$
 (9)

300 301

302

303

304

305

306

307

308 309 where the explicit latitudinal dependency on  $\phi$  is assumed to arise solely due to the geometrical effect of changes in mean annual solar zenith angle. Note that other properties, such as absorption of shortwave radiation by atmospheric water vapor (e.g. Picnus et al., 2015) and atmospheric scattering, will affect clear sky planetary albedo with latitude but are not considered in this simplified relation. The impacts of this simplification on the results are discussed below. Observations reveal how monthly-climatology  $\alpha_{ClearSky}$  varied seasonally and spatially during the period 2003-2023 (Fig. 3), with generally high values for high-latitude snow and ice covered regions and lower values over sea and vegetation-covered land regions. The annual-mean values of local clear sky albedo for the 2003-2023 climatology,  $\alpha_{ClearSky}$ , reflect

differences due to annual mean surface temperature, latitude and whether the local region is land or sea (Fig. 5a, grey and green).

Now consider the functional forms for annual-mean albedo at some specified spatial coordinates in terms of latitude and surface temperature over land and ocean. The latitudinal dependence of albedo is assumed to arise due to the change in solar zenith angle affecting the amount of incident light reflected at any given time, and across a year. The annual-mean planetary albedo for surface-type j at latitude  $\phi$ ,  $\alpha_j(\phi)$ , is assumed to be related to the planetary-mean albedo for a planet covered entirely by the same surface-type j,  $\overline{\alpha}_j$ , via a relation containing a second order Legendre polynomial in  $\sin \phi$  after Goodwin and Williams (2023), with an additional coefficient added here,  $\beta$ , giving,

$$\alpha_j(\phi) = \left[1 + \left[1 - \overline{\alpha}_j\right]\beta \left[\frac{1}{2}\left[3\sin^2\phi - 1\right]\right]\right]\overline{\alpha}_j \tag{10}$$

The additional coefficient  $\beta$  is a tunable parameter within the range  $0 \le \beta \le 1$ , where 0 indicates no latitudinal dependence on albedo for surface-material j due to latitudinal geometry and 1 indicates the maximum possible latitudinal dependence. Note that when both constraints  $0 \le \beta \le 1$  and  $0 \le \overline{\alpha}_j \le 1$ , eq. (10) implies physically plausible values for local albedo,  $0 \le \alpha_j(\phi) \le 1$ , for all  $\phi$ . The second order Legendre polynomial sine of latitude is able to accurately account for how the annual-mean solar zenith angle by the Earth with latitude (e.g. Hartmann, 1994), providing some confidence for its application (with altered coefficients) to account for how annual-mean solar zenith angle affects albedo with latitude (Goodwin and Williams, 2023).

The annual-mean local albedo is generally higher for cold regions that are covered in snow and ice most or all of the year, and generally lower for warmer regions that are ice- and snow-free for most of the year (Fig. 5a). Applying eq. (10) to each annual-mean local albedo value ( $\alpha_j$ : Fig. 3a) would then reveal the effective planetary-mean albedo for a planet entirely covered by the surface material found at that location ( $\overline{\alpha_j}$ ). This approximation is assumed here to effectively strip away the latitudinal impact on local surface albedo, and leave only the temperature and land or ocean factors. To do this, we must first identify a value for  $\beta$ . The method adopted is to assume a functional form for the temperature impact on local annual albedo, and then fit the value of  $\beta$  and the coefficients in the adopted functional form for temperature to best fit the observations.

How should temperature impact surface albedo? Here, we assume that when the ocean warm enough to be ice-free all year, then increasing the temperature further has no impact on local albedo. Therefore, the reduction in local albedo over the ocean as temperatures warm from 280 K to 300 K is assumed here to be a latitudinal geometry effect arising from variation in mean annual solar zenith angle (Fig. 5a, grey), consistent with previous observational analysis of sea surface albedo with solar zenith angle (Payne, 1972). Similarly, we assume that when the land is cold enough to be ice-covered all year, that reducing the temperature further has no

impact on local albedo. Therefore, the increase in local albedo when annual land temperatures

reduce from 245 K to 220 K (Fig. 5a, green) is assumed here to be a latitudinal geometry effect.

We seek a functional form that, on an  $\overline{\alpha}_I$ - $T_S$  plot has a low dependence at high and low

temperatures, with high  $\overline{\alpha}_I$  at low  $T_S$  and low  $\overline{\alpha}_I$  at high  $T_S$ , and has a continuous and

differentiable form between these limiting values (e.g. Fig. 5b, lines).

357

358 The temperature dependence of the planetary albedo for a planet entirely covered by either

land or ocean,  $\overline{\alpha_{ClearSky,k}}$ , is assumed to be represented by a relation containing the error

function with respect to annual mean surface temperature via (e.g. Fig. 5b, lines)

360361

366

367

369

$$\overline{\alpha_{ClearSky,k}}(T_S) = \left(\frac{\overline{\alpha_{warm,k}} + \overline{\alpha_{cold,k}}}{2}\right) - \left(\frac{\overline{\alpha_{cold,k}} - \overline{\alpha_{warm,k}}}{2}\right) \operatorname{erf}\left(\frac{T_S - (T_{warm,k} + T_{cold,k})/2}{(T_{warm,k} - T_{cold,k})/2}\right)$$
(11)

where k indicates either land or ocean,  $\overline{\alpha_{warm,k}}$  is the planetary mean albedo covered in surface k held at temperatures with no snow or ice,  $\overline{\alpha_{cold,k}}$  is the planetary mean albedo for

surface k held at temperatures where there is snow or ice all year,  $T_{warm,k}$  is the annual mean

temperature above which the surface has very little snow or ice at any time of year, and  $T_{cold,k}$  is

the annual mean temperature below which the surface is almost entirely snow or ice covered

368 all year.

Closures (10) and (11) have tunable parameters  $\beta$ ,  $\overline{\alpha_{warm,land}}$ ,  $\overline{\alpha_{cold,land}}$ ,  $\overline{\alpha_{warm,ocean}}$ ,

 $\overline{\alpha_{cold,ocean}}$ ,  $T_{warm,land}$ ,  $T_{cold,land}$ ,  $T_{warm,ocean}$  and  $T_{cold,ocean}$ . These parameters are tuned to

minimize the root of mean squares error in how eqs. (10) and (11) estimate  $\overline{\alpha_{ClearSky,k}}$  from

observed climatology (Table S1; Fig. 5b, compare lines to dots). Note that in this parameter

tuning, firstly a single value of  $\beta$  is assumed to apply to both land and ocean, and secondly it is

assumed that  $\overline{\alpha_{cold,ocean}} = \overline{\alpha_{cold,land}}$  as there are no data points with very low surface

temperatures above the ocean, and very cold conditions are assumed to be entirely ice or snow

covered all year regardless of whether they are over land or ocean.

377378379

380

The climatological annual-mean albedo values for 2003-2023 (Fig. 5a, green for land grey for ocean) are converted into the planetary mean albedo for a planet covered entirely in that surface (Fig. 5b), using the tuned value of  $\beta = 0.39$  and eq. (10),

381 382

383

384

386 387

388

392

$$\alpha_{ClearSky}(x, y, T_S) = \left[1 + \left[1 - \overline{\alpha_{ClearSky}}(x, y, T_S)\right]\beta \left[\frac{1}{2}\left[3\sin^2\phi - 1\right]\right]\right]\overline{\alpha_{ClearSky}}(x, y, T_S)$$
(12)

These relations, eqns. (10-12) with the tuned values of  $\overline{\alpha_{warm,land}}$ ,  $\overline{\alpha_{cold,land}}$ ,  $\overline{\alpha_{warm,ocean}}$ ,

 $\overline{lpha_{cold,ocean}}$ ,  $T_{warm,land}$ ,  $T_{cold,land}$ ,  $T_{warm,ocean}$  and  $T_{cold,ocean}$ , predict the annual mean

planetary albedo over each 1°x1° surface location based on the annual mean surface

temperature (Fig. 5b, compare lines to dots). The statistical models (eqns. 10, 11; Fig. 5b,

compare lines to dots) with tuned parameters (Table S1) have  $R^2$ =0.941 for  $\overline{\alpha_{ClearSkv}}(x, y, T_S)$ 

over the ocean clear sky albedo and  $R^2$ =0.919 over land, and predict  $\overline{\alpha_{ClearSky}}(x, y, T_S)$  values

that range from 0.10 to 0.62 with a root mean square error of 0.0251 over the ocean and

0.0506 over land (Fig. 3). The annual clear sky albedo  $\alpha_{ClearSky}(x, y, T_S)$  ranges from 0.09 to

0.70 and is spatially well predicted from  $T_s$ , k and  $\phi$  by the empirical relations (eqns. 9-12; Fig. 3, top row) with an overall r.m.s. error of 0.04. The largest local errors on land arise in desert and grassland regions, which have higher local clear sky albedo than other land regions at the same temperature, and in the ocean arise at the northernmost edge of the Southern Ocean sea-ice extent, where local clear sky albedo is slightly underestimated in the empirical predictions (Fig. 3).

The functions adopted here to describe the latitudinal and temperature impacts on clear sky albedo (eqns. 10, 11) are reasonable since:

- (1) The single fitted value of  $\beta=0.39$  produces the correct equatorial to high-latitude variation in *clear sky* albedo over the ocean (Fig. 3, top row, consider regions warm enough to remove any significant sea ice) and the correct equatorial to high-latitude variation in *sea surface* albedo in the Atlantic Ocean analyzed by Payne (1972) (see Supporting Information S3: Payne (1972) observes annual equatorial sea surface albedo of 0.06 increasing to between 0.09 and 0.10 for +70° to +80° latitude, in line with eq. (10) using  $\beta=0.39$  and  $\overline{\alpha}_j$  tuned to give equatorial albedo of 0.06). This agreement indicates that the latitudinal variation observed is explainable primarily due to a solar zenith angle geometry affecting the planetary surface reflection as assumed in the equations, and not a latitudinal variation in atmospheric absorption since this does not affect *sea surface* albedo;
- (2) The single fitted value of  $\beta=0.39$  removes any significant slope in planetary clear sky albedo with temperature at both warm locations, for ocean and land, and cold locations, over land (compare Fig. 5b to Fig. 5a, green and grey dots), showing that the latitudinal geometry impact on local clear sky albedo is accurately accounted for across different surface types; and (3) The fitted parameter values (Table S1) are able to accurately calculate the planetary albedo calculated for each location with low rms error (Fig. 5b, compare lines to dots), showing that the surface temperature impact on albedo is accurately accounted for.

There is more error in the land reconstruction than for the ocean, in part since the land has very warm regions that are dry and so have low vegetation and high albedo (Fig. 5). The functional equations chosen are only intended to account for the cryosphere impact on albedo with temperature, not the impact from the drying out of soils and changing of the vegetation state.

 The annual mean clear sky albedo  $\alpha_{ClearSky}$  ranges from 0.09 to 0.70 (Fig. 5a), while the implied global annual mean clear sky albedo if the entire planet was covered in that surface material  $\overline{\alpha_{ClearSky}}$  ranges from 0.10 to 0.62 (Fig. 5b). The range in  $\alpha_{ClearSky}$  is due to both surface temperature (via the cryosphere extent) and solar zenith angle, while  $\overline{\alpha_{ClearSky}}$  has the solar zenith angle effect removed. The reduced range in  $\overline{\alpha_{ClearSky}}$  compared to  $\alpha_{ClearSky}$  implies that some 85% of the observed range in clear sky albedo is functionally related to surface temperature, while 15% is due to variation in factors that co-vary with temperature in space but would not co-vary with surface temperature in time following perturbation, such as the solar zenith angle change with latitude.

# 2.2.2 Outgoing Longwave radiation for Clear Sky

Simplified functional relationships are now assessed for clear sky planetary emissivity in terms of surface temperature and other climate properties. Based on simple physical considerations, we expect that clear sky planetary emissivity,  $\varepsilon_{ClearSky}$ , will decrease with:

- an increase in surface temperature  $T_S$ , since warmer air holds more water vapor;
- an increase in surface relative humidity  $H_{rel}$ , since water vapor is a greenhouse gas;
- an increase in the height of the tropopause above the surface,  $z_{trop} z_s$ , since a higher tropopause indicates that water vapor extends to a greater height in the atmosphere and reflects changes to the lapse rate;
- an increase in surface pressure,  $p_s$ , since this indicates a greater mass of atmosphere above the surface, and so greater greenhouse effect.

Based on these physical considerations, we postulate a simplified linearized relationship whereby planetary emissivity is linearly related to surface temperature,  $T_S$ ; surface relative humidity,  $H_{rel}$ ; the height of the tropopause above local surface elevation,  $z_{trop}(x, y, t) - z_S(x, y)$ ; and surface pressure,  $p_S$ , via,

$$\varepsilon_{ClearSky}(x, y, t) \approx c_o + c_1 T_S(x, y, t) + c_2 H_{rel}(x, y, t) + c_3 [z_{trop}(x, y, t) - z_S(x, y)] + c_4 p_S(x, y, t)$$
(13)

For monthly mean observed climatology from 2003-2023 on a 1° by 1° spatial resolution, the coefficients for eq. (13) are fitted (Table S2). The empirically constrained simplified relation calculates  $\varepsilon_{ClearSky}(x,y,t)$  across all 12 months and each 1° by 1° location with a root of mean squares error of 0.0259, and has an adjusted R² value of 0.907, thus providing accurate monthly spatial estimates of planetary clear sky emissivity (Fig. 2, top two rows). In addition to producing predictions in agreement observations (Fig. 2), if the simple physical justification for eq. (13) holds then we should also expect that the empirically fitted coefficient values  $c_1$ ,  $c_2$ ,  $c_3$  and  $c_4$  should all be negative, which they are (Table S2).

The coefficient  $c_1$  takes the value  $c_1 = \frac{\partial \varepsilon_{ClearSky}}{\partial T_S} = -(2.935 \pm 0.003) \times 10^{-3} \, \text{K}^{-1}$  when (13) is empirically fitted to data on a monthly climatological basis (Supplementary Table S2), indicating that 78% of the observed spatial variation in  $\varepsilon_{ClearSky}$  with  $T_S$  ( $\frac{\delta \varepsilon_{ClearSky}}{\delta T_S} = -3.75 \times 10^{-3} \, \text{K}^{-1}$ : Fig. 4e) is functionally due to variation in surface temperature, whereas 22% of the observed variation is due to variation in factors that co-vary with temperature in space but would not covary with surface temperature in time following perturbation. For example, spatial locations with high surface elevation and low surface pressure are generally also cold and have high planetary emissivity,  $\varepsilon_{ClearSky}$ . There is also a near-linear relationship between  $L_{out}$  and  $T_S$  in the region of parameter space considered (Fig. 2c,e), implying that up to around 78% of the spatial variation in outgoing longwave radiation at the top of the atmosphere is functionally related to surface temperature.

# 2.3 TOA outgoing radiation in all sky conditions

# 2.3.1 Outgoing Shortwave for All Sky

Now, the impact of clouds on the planetary albedo is assessed to constrain a relation for albedo feedback under all sky conditions. The albedo of clouds is evaluated using a model of how clouds either reflect or emit radiation, and the surface of the planet reflects radiation, leading to an infinite series of emission and reflection contributions (Supporting Information Text S1 and Fig. S1). A key difference relative to previous infinite series models (e.g. Taylor et al., 2007) is that here a distinction is made between the albedo of cloud for incident solar radiation (which is assumed to be latitudinally dependent due to changes in mean solar zenith angle) and the albedo of cloud for diffuse upwards radiation that has been reflected by the Earth's surface (which is assumed to be latitudinally independent).

Adopting this separation of directed and diffuse albedo model (Supporting Information Text S1 and Fig. S1), the cloudy sky albedo is related to the clear sky albedo via,

$$\alpha_{CloudySky}(x,y) \approx \alpha_{Cloud:dir}(x,y) + \overline{\alpha_{ClearSky}}(x,y) \frac{[1 - \alpha_{Cloud:dir}(x,y)][1 - \overline{\alpha_{Cloud}}]}{[1 - \overline{\alpha_{ClearSky}}(x,y) \times \overline{\alpha_{Cloud}}]}$$
(14)

where  $\alpha_{Cloud:dir}(x,y)$  is the annual mean albedo of cloud at location x,y for directed incident solar radiation,  $\overline{\alpha_{Cloud}}$  is the global mean cloud albedo, which is assumed equal to the albedo of cloud for diffuse radiation from below and is invariant with latitude. Using observational estimates for  $\alpha_{CloudySky}(x,y)$  (Fig. 3) and modifying observed  $\alpha_{ClearSky}(x,y)$  with eq. (12) to obtain  $\overline{\alpha_{ClearSky}}(x,y)$ , eq. (14) is iteratively solved to calculate the climatological spatial pattern of cloud albedo for directed solar radiation,  $\alpha_{Cloud:dir}(x,y)$ , for the period 2003-2023 (Figure 6, right hand column), noting that  $\overline{\alpha_{Cloud}}$  is the global average cloud albedo.

 The local variations in reconstructed cloud albedo,  $\alpha_{Cloud:dir}$ , reflect differences in cloud properties (Fig. 6). However, within this variation due to local cloud properties, the evaluated values of  $\alpha_{Cloud:dir}(x,y)$  show a general pattern of increasing with latitude  $\phi$  (Fig. 6, right hand side), consistent with the Stephens (1978) theoretical model and parameterization identifying how the magnitude of cloud albedo varies with solar zenith angle (see Stephens, 1978, Figure 4 therein).

#### 2.3.2 Outgoing Longwave for All Sky

Now, the impact of clouds on the relationship between clear sky planetary emissivity and surface temperature is considered. Clear sky planetary emissivity  $\varepsilon_{ClearSky}$  is empirically related to surface temperature via equation (13). However, to calculate longwave climate feedbacks in all sky conditions, we need to relate planetary emissivity in all sky conditions,  $\varepsilon_{AllSky}$ , to  $\varepsilon_{ClearSky}$ .

With no atmosphere, and a perfect blackbody surface, the planetary emissivity would be equal to 1. In clear sky conditions planetary emissivity is less than 1 because greenhouse gasses in the atmosphere reduce the TOA outgoing longwave radiation compared to the expected emission from the surface (Fig. 2, left hand column): the ambient reduction in planetary emissivity in clear sky conditions is  $1 - \varepsilon_{ClearSky}$ . This ambient planetary emissivity is reduced further in the presence of clouds because clouds themselves reduce TOA outgoing radiation (Fig. 2, compare middle and left hand columns): the total reduction in planetary emissivity with clouds and an atmosphere is  $1 - \varepsilon_{CloudySky}$  (Supplementary Figure S2).

Since clouds reduce outgoing longwave radiation at the TOA, a recent study (Goodwin and Williams, 2023) expressed this reduction of planetary emissivity due to clouds of clouds via a cloud-emissivity coefficient,  $c_{\varepsilon} = \left[1 - \varepsilon_{CloudySky}\right]/\left[1 - \varepsilon_{ClearSky}\right]$ , where  $c_{\varepsilon}$  is an amplification factor by which the value of one minus the emissivity for clear sky conditions is amplified in cloudy sky conditions. The value of  $c_{\varepsilon}$  represents the impact of clouds on the longwave radiation budget and varies with cloud type.

Here, we utilize this cloud-emissivity coefficient to relate  $\varepsilon_{AllSky}$  to  $\varepsilon_{ClearSky}$  and parameters representing cloud amount,  $f_{CA}$ , and cloud type,  $c_{\varepsilon}$ , of the form

536 
$$\varepsilon_{AllSky} = \varepsilon_{ClearSky} - f_{CA}(c_{\varepsilon} - 1)(1 - \varepsilon_{ClearSky})$$
 (15)

where the cloud-emissivity coefficient (Goodwin and Williams, 2023) expresses the longwave radiation budget impact of clouds via,

$$c_{\varepsilon}(x,y,t) = \frac{\left[1 - \varepsilon_{CloudySky}(x,y,t)\right]}{\left[1 - \varepsilon_{ClearSky}(x,y,t)\right]}$$
(16)

Here, the cloud emissivity coefficient of Goodwin and Williams (2023), is re-analyzed for the 2003-2023 period, using monthly climatology at 1° by 1° spatial resolution (Fig. 6, left hand panels). The resulting values of  $c_{\varepsilon}$  for across each 1° by 1° gridpoint in each month have a median value of  $c_{\varepsilon}=1.23$ , 66% of values between 1.11 and 1.34 and 90% of values between 1.05 and 1.42 (Fig. 6, left hand panels). Therefore, the value of  $1-\varepsilon_{CloudySky}$  is larger than  $1-\varepsilon_{ClearSky}$  by between 5 and 42% across spatial and monthly variation for 90% of the time. Note that the variation in  $c_{\varepsilon}$  values arises for local climate states with very different monthly climatologies, with large variation in surface temperatures, relative humidites, surface elevations and other climatological parameters including cloud type.

Combining the empirical prediction for clear sky planetary emissivity ( $\varepsilon_{ClearSky}$ ; eq. 13; Fig. 2) with the observed spatial monthly climatology for the cloud emissivity coefficient ( $c_{\varepsilon}$ ; eq. 16; Fig. 6), and accounting for observed cloud amount using eq. (7a), produces an empirical relation for all sky planetary emissivity,  $\varepsilon_{AllSky}(x,y,t)$  (eq. 15; Figure 2, bottom two rows), where the empirical prediction in Fig. 2 uses  $\varepsilon_{ClearSky}$  values predicted from eq. (13) and  $f_{CA}$  and  $c_{ep}$  as observed from monthly climatology. This empirical prediction for spatial and monthly all sky

emissivity is in good agreement with the observed values (Fig. 2), with an r.m.s. error of 0.03 (Fig. 2, bottom two rows). There is significant local error in isolated cold polar locations where  $\varepsilon_{ClearSky}(x, y, t)$  is close to 1, and the denominator of eq. (16) goes to zero.

562563564

565

566

567

# 3. Climate feedbacks

The simplified functional relationships for planetary emissivity and planetary albedo to calculate the Planck, WVLR and albedo climate feedbacks in clear sky and all sky conditions are now utilized. Cloud feedbacks are not considered. From eqns. (1), (2) and (7), the local climate feedback for sky-condition i at location x, y is defined as,

568569

570 
$$\lambda_i(x,y) = -\frac{\partial R_{out,i}}{\partial T_S}(x,y) = -\frac{\partial}{\partial T_S} \left[ \varepsilon_i(x,y) \sigma T_S^4(x,y) + \alpha_i(x,y) R_{in}(x,y) \right]$$
 (17a)

571

572 which differentiates giving,

573

574 
$$\lambda_{i}(x,y) = -\underbrace{4\varepsilon_{i}(x,y)\sigma T_{S}^{3}(x,y)}_{Planck} - \underbrace{\sigma T_{S}^{4}(x,y)\frac{\partial\varepsilon_{i}}{\partial T_{S}}(x,y)}_{WVLR+LWcloud} - \underbrace{R_{in}(x,y)\frac{\partial\alpha_{i}}{\partial T_{S}}(x,y)}_{albedo+SWCloud}$$
(17b)

575

- 576 To remove the cloud feedbacks from eq. (17) we set in this study the partial derivatives of
- 577 emissivity and albedo with surface temperature to be evaluated without a temporal change in
- 578 cloud amount, cloud emissivity coefficient or cloud albedo, such that
- 579  $\frac{\partial \varepsilon_i}{\partial T_S} = \frac{\partial \varepsilon_i}{\partial T_S} \bigg|_{\delta f_{CA} = \delta c_\varepsilon = \delta \alpha_{Cloud} = 0} \text{ and } \frac{\partial \alpha_i}{\partial T_S} = \frac{\partial \alpha_i}{\partial T_S} \bigg|_{\delta f_{CA} = \delta c_\varepsilon = \delta \alpha_{Cloud} = 0}.$  The consequences of changes
- in cloud amount and cloud properties (via cloud emissivity coefficient and cloud albedo) with time are reserved for future study.

581 582

583

Analyzing the global mean climate feedback for some process and cloud state  $\overline{\lambda}_i$  then requires convoluting this spatial feedback (eq. 17) with a warming pattern,

584 585

$$\overline{\lambda}_{t} = \frac{\int \lambda_{t}(x, y) \Delta T_{S}(x, y) dx dy}{\int \Delta T_{S}(x, y) dx dy}$$
(18)

587

- Here, we use the multi-model warming pattern for a 2°C global-mean warming from
- Assessment Report 6 of the Intergovernmental Panel on Climate Change (IPCC, 2021). The
- associated 4°C warming pattern (IPCC, 2021) is also used to assess how climate feedbacks vary
- 591 with the background climate state, by re-analyzing the climate feedback for surface
- temperature profiles of +2 K and +4 K warming (calculated as the ERA5 temperature profile for 1940-1960 with the +2 K and +4 K IPCC (2021) warming patterns).

594

595

# 3.1 Planck feedback

The Planck feedback is defined here as the change in outgoing radiation following a change in surface temperature while atmospheric planetary emissivity is held constant (to represent

constant atmospheric constituents). The Planck feedback for clear skies is written, from eq. (11),

$$\lambda_{Planck,ClearSky}(x,y) = -4\varepsilon_{ClearSky}(x,y)\sigma T_S^3(x,y)$$
(19)

while the Planck feedback for all sky conditions is,

The clear-sky albedo feedback is written, from eq. (17),

$$\lambda_{Planck,AllSkv}(x,y) = -4\varepsilon_{AllSkv}(x,y)\sigma T_S^3(x,y)$$
(20)

Using monthly mean climatology for the period 2003-2023, the Planck feedback is analyzed, giving a global spatial average of  $\lambda_{Planck,ClearSky} = -3.72 \text{ Wm}^{-2}\text{K}^{-1}$  and  $\lambda_{Planck,AllSky} = -3.33 \text{ Wm}^{-2}\text{K}^{-1}$  for uniform surface warming. When convoluted with a multi-model mean pattern for 2°C global warming (IPCC, 2021), the 2003-2023 all sky Planck feedback becomes  $\lambda_{Planck,AllSky} = -3.30 \text{ Wm}^{-2}\text{K}^{-1}$ . This Planck feedback analysis is similar to previous methods (e.g. see Sherwood et al., 2020), and correspondingly gives similar results (Table 1).

3.2 Surface albedo feedback

$$\lambda_{albedo,ClearSky}(x,y) = -R_{in}(x,y) \frac{\partial \alpha_{ClearSky}}{\partial T_S}(x,y)$$
 (21)

The clear sky surface albedo feedback,  $\lambda_{albedo,ClearSky}(x,y)$ , is now evaluated by differentiating  $\alpha_{ClearSky}$  with respect to surface temperature and substituting into the relevant term in eq. (17). The partial derivative of local clear sky albedo respect to surface temperature is evaluated via,

625 
$$\frac{\partial \alpha_{ClearSky}}{\partial T_S}(x,y) = \left[1 + \beta \left[\frac{1}{2} \left[3\sin^2 \phi - 1\right]\right]\right] \frac{\partial \overline{\alpha_{ClearSky}}}{\partial T_S}(x,y)$$
 (22)

where  $\frac{\partial \overline{\alpha_{ClearSky}}}{\partial T_S}(x,y)$  is the partial derivative of eq. (11) with respect to surface temperature, adopting the fitted parameter values over land and ocean (Table S1).

- From our simplified relationships constrained by observed climatology for 2003-2023, the
- annual mean local clear sky albedo feedback (eq. 21: Fig. 7a) reveals high values in the
- 636 Himalayas and high latitude regions where a small temperature change would lead to a large
- variation in surface albedo. The zonal mean values evaluated from simplified theory and
- observations here (Fig. 7c, blue) show similarities to the values evaluated for CMIP6 models

using radiative kernels following a 4xCO<sub>2</sub> perturbation (Fig. 7c, grey), both in terms of the maximum magnitude and also the zonal pattern.

640 641 642

643 644

639

- Three key differences arise from the spatially-derived method used here (Fig. 7a, 7c blue) compared to the standard temporally-derived radiative kernel method applied to CMIP6 models (Fig. 7c, grey):
- (1) The method here evaluates the feedback from observations within a reduced physics 645 framework, whereas the radiative kernel method is applied to climate models that contain 646 complex physics but may also contain model bias; 647
- (2) The method here considers only the cryosphere impact on clear sky albedo, and does not 648 consider any vegetation-induced albedo changes, whereas CMIP6 models with coupled 649 650 vegetation will include both cryosphere and vegetation induced surface albedo changes; and (3) The method here evaluates  $\lambda_{albedo,ClearSky}(x,y)$  for an infinitesimal perturbation to the 651 climate state (eq. 21), whereas the radiative kernel approach applies to a large finite 4xCO<sub>2</sub> 652 perturbation. Where snow or ice melts early in the large 4xCO<sub>2</sub> perturbation, this finite 653 approximation will reduce the temporally derived climate feedback relative to an infinitesimal 654
- perturbation, since the change in albedo will be the same but the change in the denominator 655 (surface temperature) will be larger.

656

657 658 659

660

661

662

663

664

665

666

Anthropogenic forcing is warming future climate beyond an infinitesimal perturbation (IPCC, 2021). To explore large perturbations, our method evaluates  $\lambda_{albedo,ClearSky}(x,y)$  for infinitesimal perturbations applied to warmed climate states, using surface temperature patterns for +2K and +4K global mean warming (IPCC, 2021) added on to the 1940-1960 climatological mean in the ERA5 surface temperature record (the earliest period within the ERA5 dataset used). This choice results in reduced  $\lambda_{albedo,ClearSky}(x,y)$  for the warmed climate states relative to the 2003-2023 period, especially in northern high latitudes where the cryosphere is in retreat (Figure 7c, compare orange and red to blue). This response explains the higher  $\lambda_{albedo}$  values obtained from our method relative to 4xCO<sub>2</sub> perturbation in CMIP6 models

667 668 669

670

671

672

Uncertainties in  $\lambda_{albedo.ClearSky}(x, y)$  are estimated from scaling arguments from the error in  $\overline{\alpha_{ClearSky}}(x, y, T_S)$  divided by the range of  $\overline{\alpha_{ClearSky}}(x, y, T_S)$ : the fractional uncertainty in  $\lambda_{albedo,ClearSky}(x,y)$  is estimated as the root mean square error in  $\overline{\alpha_{ClearSky}}(x,y,T_S)$  divided by the maximum range of  $\overline{\alpha_{ClearSky}}(x, y, T_S)$  over land and ocean (Fig. 5c, blue, red and orange shading).

673 674 675

676

To calculate the surface albedo feedback in all sky conditions, without considering changes in cloud amount or cloud properties,

677 678

$$\lambda_{albedo,AllSky} = -R_{in} \frac{\partial \alpha_{AllSky}}{\partial T_S}$$
 (23)

we now calculate  $\frac{\partial \alpha_{AllSky}}{\partial T_S}$  , by considering the impact of cloudy skies and non-zero cloud

amount on  $\frac{\partial \alpha_{ClearSky}}{\partial T_S}$  (eq. 22). The partial derivative of cloudy sky albedo is related to the

partial derivative of clear sky albedo via differentiating eq. (14) (Supporting Information S1),

$$\frac{\partial \alpha_{CloudySky}}{\partial T_S} = \left[ \frac{[1 - \alpha_{Cloud:dir}(x, y)][1 - \overline{\alpha_{Cloud}}]}{[1 - \overline{\alpha_{ClearSky}}(x, y)\overline{\alpha_{Cloud}}]^2 [1 + \beta[0.5 \times [3\sin^2\phi - 1]]]} \right] \frac{\partial \alpha_{ClearSky}}{\partial T_S}$$
(24)

The partial derivatives of albedo with respect to surface temperature in clear sky, all sky and cloudy sky conditions are related, from eq. (7), via,

691 
$$\frac{\partial \alpha_{AllSky}}{\partial T_S} = f_{Cl} \frac{\partial \alpha_{CloudySky}}{\partial T_S} + [1 - f_{Cl}] \frac{\partial \alpha_{ClearSky}}{\partial T_S}$$
 (25)

By substituting (24) and (25) in (17) the surface albedo feedback in all sky conditions becomes,

695 
$$\lambda_{albedo,AllSky} = -R_{in} \left[ f_{CI} \frac{\left[1 - \overline{\alpha_{Cloud}}\right] \left[1 - \alpha_{Cloud:dir}\right]}{\left[1 - \overline{\alpha_{Cloud}}\right]^{2} \left[1 + \beta \left[0.5 \times \left[3 \sin^{2} \phi - 1\right]\right]\right]} + \left[1 - f_{CI}\right] \right] \frac{\partial \alpha_{ClearSky}}{\partial T_{S}}$$
696 (26)

The values of  $\lambda_{albedo,AllSky}$  are calculated for surface temperatures during the 2003-2023 period (Fig 7b,d), and also for +2K and +4K warmed climate states (Fig. 7d). The  $\lambda_{albedo,AllSky}$  for each level of warming is correspondingly reduced relative to  $\lambda_{albedo,ClearSky}$ , and the  $\lambda_{albedo,AllSky}$  values derived here from observations and simplified theory are similar to the CMIP6 derived values using radiative kernels and a 4xCO<sub>2</sub> perturbation (Fig. 7d). Uncertainty in  $\lambda_{albedo,AllSky}$  is estimated through the application of the same scaling arguments as adopted for  $\lambda_{albedo,ClearSky}$  (Fig. 7c,d, blue, red and orange shading).

The global mean surface albedo feedback in all sky conditions is 0.6 (0.53 to 0.66 at 66% confidence) Wm<sup>-2</sup>K<sup>-1</sup> for 2003-2023 background surface temperatures, decreasing to 0.5 (0.45 to 0.55) Wm<sup>-2</sup>K<sup>-1</sup> if background surface temperatures had already undergone +2K warming (Table 1) and decreasing to 0.32 (0.28 to 0.35) Wm<sup>-2</sup>K<sup>-1</sup> for 4K warming.

# 3.3 Water Vapor Lapse Rate feedback

The water vapor-lapse rate (WVLR) feedback is defined here as the change in outgoing longwave radiation per unit warming due to a change in the planetary emissivity of the

atmosphere following a change in climate state. From eq. (17) the WVLR feedback for clear

715 skies is

716 
$$\lambda_{WVLR,ClearSky}(x,y) = -\sigma T_S^4(x,y) \frac{\partial \varepsilon_{ClearSky}}{\partial T_S}(x,y)$$
 (27)

- We now need to evaluate  $\frac{\partial \varepsilon_{ClearSky}}{\partial T_S}$  by differentiating the observation-constrained reduced
- physics relation for  $\varepsilon_{ClearSky}$ , eq. (13). Assuming that the changes in tropospheric height,
- surface relative humidity and surface pressure with a change in climate state alter planetary
- emissivity significantly less than the change in surface temperature, then the partial derivative
- 723 becomes,

$$725 \qquad \frac{\partial \varepsilon_{ClearSky}}{\partial T_S} \approx c_1 \tag{28}$$

726

- This simplification is a good approximation so long as  $\left| \frac{\partial z_{trop}}{\partial T_S} \frac{\partial \varepsilon_{ClearSky}}{\partial z_{trop}} \right|$ ,  $\left| \frac{\partial H_{rel}}{\partial T_S} \frac{\partial \varepsilon_{ClearSky}}{\partial H_{rel}} \right|$  and
- $\frac{\left|\frac{\partial p_S}{\partial T_S}\frac{\partial \varepsilon_{ClearSky}}{\partial p_S}\right|}{\partial p_S} \text{ are each much smaller than } \left|\frac{\partial \varepsilon_{ClearSky}}{\partial T_S}\right|, \text{ (eq. 6), reflecting how the changes in }$
- tropospheric height, surface relative humidity and surface pressure with a change in climate
- state alter planetary emissivity significantly less than the change in surface temperature.

731

- Substituting (28) into (27), and using the constrained value of  $c_1 = \frac{\partial \varepsilon_{ClearSky}}{\partial T_S} = -(2.935 \pm 1.00)$
- 733  $0.003) \times 10^{-3} \text{ K}^{-1}$ , gives  $\lambda_{WVLR,ClearSky}$  varying from approximately 0.5 Wm $^{-2}$ K $^{-1}$  in cold regions
- to 1.5 Wm<sup>-2</sup>K<sup>-1</sup> in warm regions (Fig. 8, left hand column).

735

- Uncertainty in the value of  $\lambda_{WVLR,ClearSky}$  is due to our assumption that  $\varepsilon_{ClearSky}$  is related to
- $T_S$  via a linear term in eq. (13),  $c_1T_S$ . The observed relation between spatial variation in
- $\varepsilon_{ClearSky}$  and  $T_S$  in modern climatology does reveal an approximate linear relation (Fig. 4e),
- which informs the decision to assume a linear term in eq. (13) as a best estimate for the
- functional relationship. However, a non-linear relationship is still possible. Supporting
- Information S2 evaluates the uncertainty in  $\lambda_{WVLR,ClearSky}$  that arises from the introduction of
- 742 a non-linear term between  $\varepsilon_{ClearSky}$  and  $T_S$  via modification of eq. (13), whereby the  $c_1T_S$  term
- becomes  $c_1T_S^n$ . The systematic uncertainty in  $\lambda_{WVLR,ClearSky}$  arising from the linear assumption
- is evaluated in assuming that the value of the power varies with a normal distribution with
- mean 1 and standard deviation 1,  $n \sim N(1,1)$  (Supporting Information S2; Fig. 8c, blue shading).
- The relatively small systematic uncertainty introduced by the linear assumption (Fig. 8c),
- combined with the good statistical fit for eq. (13) (Figure 2; Table S2), provides confidence in
- the evaluation of  $\lambda_{WVLR,ClearSky}$  (Fig. 8a,c)

749 750

The WVLR feedback in all sky conditions is given by,

751 752

752 
$$\lambda_{WVLR,AllSky}(x,y) = -\sigma T_S^4(x,y) \frac{\partial \varepsilon_{AllSky}}{\partial T_S}(x,y)$$
 (29)

- where it is assumed that both cloud amount,  $f_{CA}$ , and cloud type are unchanging with
- perturbation. The impact on outgoing longwave radiation of cloud type is represented in this
- study by the cloud-emissivity coefficient,  $c_{\varepsilon}$  (eq. 16; Goodwin and Williams, 2023) in eq. (15),
- relating  $\varepsilon_{AllSky}$  to  $\varepsilon_{ClearSky}$ ,  $f_{CA}$  and  $c_{\varepsilon}$ . Therefore, to identify  $\frac{\partial \varepsilon_{AllSky}}{\partial T_S}(x,y)$  as a function of

 $\frac{\partial \varepsilon_{ClearSky}}{\partial T_S}(x,y)$ , we differentiate eq. (15) with respect to surface temperature holding  $f_{CA}$  and  $c_{\varepsilon}$  constant to reveal,

$$\frac{\partial \varepsilon_{AllSky}}{\partial T_S}(x,y) = \left[1 - f_{CA}(x,y) + f_{CA}(x,y)c_{\varepsilon}(x,y)\right] \frac{\partial \varepsilon_{ClearSky}}{\partial T_S}(x,y) \tag{30}$$

Substituting (30) into (29) then reveals the WVLR feedback in all sky conditions in terms of the sensitivity of clear sky planetary emissivity to surface temperature, the cloud amount area fraction, the cloud-emissivity coefficient, surface temperature and the Stefan-Boltzmann constant,

$$\lambda_{WVLR,AllSky}(x,y) = -\sigma T_S^4 [1 - f_{CA} + f_{CA} c_{\varepsilon}] \frac{\partial \varepsilon_{ClearSky}}{\partial T_S}(x,y)$$
(31)

This relation is evaluated for the observed climatology from 2003-2023, revealing  $\lambda_{WVLR,AllSky}$  spatially (Fig. 8b) and for zonal averages (Fig. 8d), where zonal averages include the systematic uncertainty from the assumption of a linear term relating  $\varepsilon_{ClearSky}$  and  $T_S$  (Fig. 8d, blue shading; Supporting Information S2). The magnitudes of zonal average  $\lambda_{WVLR,AllSky}$  are generally similar to CMIP6 model values approximated through radiative kernels and a 4xCO<sub>2</sub> temporal perturbation (Fig. 8d), but show a smoother latitudinal variation. This may reflect a difference between how cloud amount and type are held constant between the methodologies ( $\delta c_{\varepsilon} = 0$  and  $\delta f_{CA} = 0$  here versus imposed constant simulated cloud amount and type in the CMIP6 simulations). These different methodologies may then imply differences in how clouds interact with non-cloud features of the air column that are changing with perturbation (e.g. water vapor content, aerosols) to affect longwave radiation.

The global mean all sky WVLR feedback is 1.30 (1.20 to 1.40) Wm<sup>-2</sup>K<sup>-1</sup> for the 2003-2023 surface temperatures (Table 1). Our analysis suggests that the WVLR feedback only increases a small amount as the world warms, although we note that we do not have a strong constraint on the second derivative of planetary emissivity with surface temperature from our observationally constrained functional relationship (eq. 13, Supporting Information S2). Therefore, we have low confidence in the WVLR feedback evaluation for the +2 K and +4 K warmed worlds.

# 3.4 Global mean total feedback

The global mean values of the Planck, WVLR and surface albedo feedbacks are analyzed from spatial variation for the 2003-2023 climatology combined with a +2K warming pattern (Table 1), and are similar in magnitude to values analyzed using temporal perturbation methods (IPCC, 2021; Sherwood et al., 2020; Zelinka et al, 2020). While the Planck and WVLR feedbacks are consistent (Table 1), the surface albedo feedback for the 2003-2023 climatology is larger than recent estimates for temporal variation for an infinitesimal perturbation to the 2003-2023 climatology, but is consistent with previous estimates when the world has warmed by +2K and +4K above the mid-20<sup>th</sup> century average. 

To calculate total climate feedback,  $\lambda_{total} = \Sigma \lambda_X$ , we combine our Planck, WVLR and surface albedo feedback estimates in all sky conditions with the estimate of cloud feedbacks from a recent statistical learning analysis of how clouds respond to change in environment (Ceppi and Nowack, 2021):  $\lambda_{cloud}=0.43\pm0.35~{\rm Wm^{-2}K^{-1}}$  at 90% confidence. Note that this cloud feedback estimate is similar to estimates from recent reviews of the literature (IPCC, 2021; Sherwood et al., 2020; Table 1), but with a reduced uncertainty range. We calculate the total global mean climate feedback only for the 2003-2023 climatology, since we have low confidence in the WVLR feedbacks for the +2 and +4 K warmed worlds (Table 1). Assuming independent uncertainty between terms, our analysis combined with Ceppi and Nowack (2021) provides a  $\lambda_{total} = -0.99 \,[-0.59 \,\text{to} \, -1.39 \,\text{at} \, 90\% \,\text{confidence}] \,\text{Wm}^{-2} \text{K}^{-1} \,\text{for the} \, 2003-2023 \,\text{period} \, (\text{Table})$ 1; Fig. 8a). Our spatially-derived estimates are consistent with previous temporal variation methods for calculating total climate feedback (Figure 9; Table 1: IPCC, 2021; Sherwood et al., 2020; Zelinka et al., 2020), having a similar best-estimate to the mean of the CMIP6 models and being consistent with the smaller magnitude (more amplifying) section of the climate feedback ranges of recent reviews. Note that in the Sherwood et al. (2020) review, additional evidence is used to constrain Equilibrium Climate Sensitivity (ECS) that is not used to constrain the climate feedback, and therefore the reduced range of our  $\lambda_{total}$  estimate relative to Sherwood et al (2020) (Figure 9) does not imply a similarly reduced range for ECS.

**4. Discussion** 

Many existing methods evaluate climate feedbacks from the *temporal* variation in climate state following some perturbation (e.g. Sherwood et al., 2020). When applied to numerical climate models, the temporal variation is induced by application of finite perturbations to the climate system, often with a quadrupling of atmospheric CO<sub>2</sub> (e.g. Soden et al., 2008; Zelinka et al. 2020). Observation-based methods (e.g. Cael et al., 2023; Sherwood et al., 2020; Goodwin, 2021; Goodwin and Cael, 2021) often employ the recent temporal changes in surface temperature and outgoing radiation at the top of the atmosphere, where time-mean net outgoing radiation is sometimes deduced from heat content changes in the ocean and Earth system. Paleoclimate approaches avoid the need to calculate Earth's transient energy imbalance by considering longer timescales, but do rely on proxy evidence to reconstruct the observable quantities (e.g. Rohling et al., 2018). Other approaches involving observational records include using the internal variability within observational records to constrain climate feedback (Dessler, 2013) and applying emergent constraints to assess which complex climate models have the best simulated representation of the climate's sensitivity to change (e.g. Cox et al., 2018).

This study has presented a new methodology for evaluating climate feedbacks, where simplified relations between outgoing radiation and climatological properties (eqns. 1-30) are empirically constrained with *spatial* variation in observed climatology (Hersbach et al., 2023; Loeb et al., 2018; Figs. 1-6), and then differentiated with respect to surface temperature to reveal the Planck, WVLR and surface albedo feedbacks (Figs. 7, 8). The climate feedbacks are evaluated spatially at 1° by 1° horizontal resolution, and then a global mean is found by convoluting with a spatial warming pattern.

When spatial variation is considered, both TOA outgoing longwave radiation and outgoing shortwave radiation vary considerably with surface temperature (e.g. Fig. 2c,d for clear skies), which is expressed via spatial variation in planetary emissivity and planetary albedo respectively (Fig. 2e,f). Our simplified and empirically constrained relations identify that 85% of the apparent spatial link between clear sky albedo and surface temperature arises through a functional dependance. The remaining 15% of the apparent spatial link arises through the latitudinal effect on the solar-zenith angle, which co-varies with surface temperature in space but would not co-vary with temperature in time following perturbation. Similarly, we identify that around 78% of the apparent spatial link between clear sky planetary emissivity and surface temperature arises through a functional dependence. The remaining 22% of this apparent spatial link arises through factors that co-vary with surface temperature in space but would not co-vary in time following perturbation, such as surface pressure and the height of the tropopause. Through extracting these co-varying factors, our methodology uses observed spatial variation in outgoing radiation and surface temperature to evaluate climate feedbacks following perturbation.

Our spatial-variation methodology is complementary to existing temporal-variation methods, with consistent results (Table 1) derived from independent evidence, assumptions and uncertainties. For example, the reduced physics nature of our approach contrasts with the complex climate models used for evaluating climate feedbacks in the literature (e.g. Zelinka et al., 2020). However, the ability to evaluate climate feedbacks from spatial variation in observed climatology produces a significantly better signal-to-noise ratio (with spatial temperatures and outgoing radiation varying by order 80 K and 100 Wm<sup>-2</sup>K<sup>-1</sup> respectively) when compared to historic observations of temporal changes in temperature and outgoing radiation (of order 1 K and 1 Wm<sup>-2</sup>K<sup>-1</sup> respectively). When producing an estimate of climate feedback, and the related Equilibrium Climate Sensitivity, from multiple lines of evidence using a Bayesian framework then a method that is largely independent of pre-existing methods can be useful in narrowing the overall uncertainty range (Sherwood et al., 2020), such as the method presented here (e.g. Fig. 9).

Our best estimate for global mean total climate feedback analyzed from spatial information, when using the Ceppi and Nowack (2021) cloud feedback term, comes out slightly smaller in magnitude than the IPCC (2021) AR6 and Sherwood et al. (2020) estimates: -0.99 Wm<sup>-2</sup>K<sup>-1</sup> compared to -1.16 Wm<sup>-2</sup>K<sup>-1</sup> and -1.30 Wm<sup>-2</sup>K<sup>-1</sup> respectively (Table 1). One difference in methodology is that our spatial estimate considers the albedo feedback for an infinitesimal

warming perturbation, whereas the IPCC (2021) and Sherwood et al. (2020) estimates consider a  $4xCO_2$  perturbation with relatively large finite warming. When we apply our methodology to calculate the albedo feedback for infinitesimal perturbation starting from a warmed world (Table 1; Fig. 7), there is a reduction in the positive albedo feedback by a magnitude enough to explain the difference between our estimate of total climate feedback and the IPCC (2021) and Sherwood et al (2020) estimates.

883 884

878 879

880

881

882

885

886

887

888

889

890

891

892

893

894

895

896

897

898

899

900

901

902

903

904

# Acknowledgments

The authors declare no financial conflicts of interest.

# **Open Research**

The ERA5 reanalysis (Hersbach et al., 2023) for monthly averaged data on single levels is available for download here: https://doi.org/10.24381/cds.f17050d7 (accessed 31-03-2024). The CERES Energy Balanced and filled (EBAF4.2) satellite observation dataset used here for the period 2003-2023 (Loeb et al., 2018) is available here: https://doi.org/10.5067/TERRA-AQUA-NOAA20/CERES/EBAF-TOA L3B004.2 (accessed 08/04/2024; dataset reference: NASA/LARC/SD/ASDC (2022)). CMIP data were obtained from the UK Centre for Environmental Data Analysis portal (https://esgf-index1.ceda.ac.uk/search/cmip6-ceda/; dataset reference WCRP (2024)). We acknowledge the WCRP, which, through its Working Group on Coupled Modeling, coordinated and promoted CMIP6. We thank the climate-modeling groups for producing and making available their model output, the Earth System Grid Federation (ESGF) for archiving the data and providing access and the multiple funding agencies that support CMIP6 and ESGF. Code for calculating the height of the tropopause, from Mateus et al. (2022), is available for download here: https://github.com/pjmateus/global tropopause model (accessed 14/04/2023, Model code reference Mateus et al. (2022b)); where this study uses the options for a bilinear interpolation model of the tropopause, and a surface at 3.0 potential vorticity units, where 1 potential vorticity unit is equal to 10<sup>-6</sup> K kg<sup>-1</sup> m<sup>2</sup> s<sup>-1</sup>. The GMTED2010 dataset for mean surface elevation (Danielson & Gesch, 2011) is available here: https://temis.nl/data/gmted2010/ (accessed 18/03/2024; Dataset reference USGS (2011)). The matlab code

905	developed here for conducting the analysis here is available at <a href="https://github.com/WASP-">https://github.com/WASP-</a>
906	ESM/Spatial Climate Feedback/tree/main {which will be released with a permanent doi upon acceptance of
907	this manuscript for publication; reference Goodwin et al. (2024 submitted)}. Note that the code requires
908	separate download of datasets mentioned above.
909	
910	
911	References
912	Cael, B. B., Bloch-Jonhson, J., Ceppi, P., Fredriksen, HB., Goodwin, P., Gregory, J.M., Smith, C.J.
913	& Williams, R.G. (2023), Energy budget diagnosis of changing climate feedback. Science
914	Advances 9, 16, eadf9302, doi:10.1126/sciadv.adf9302.
915	
916	Ceppi, P., and Nowack, P. (2021) Observational evidence that cloud feedback amplifies global
917	warming, Proc. Natl. Acad. Sci. U.S.A. 118 (30), e2026290118,
918	https://doi.org/10.1073/pnas.2026290118.
919	
920	Cox, P., Huntingford, C. and Williamson, M. (2018) Emergent constraint on equilibrium climate
921	sensitivity from global temperature variability, <i>Nature</i> 553, 319–322, doi:10.1038/nature25450
922	
923	Danielson, J.J., & Gesch, D.B. (2011), Global multi-resolution terrain elevation data 2010
924	(GMTED2010): U.S. Geological Survey Open-File Report 2011–1073, 26 p.
925	
926	Dessler, A. E. (2013), Observations of Climate Feedbacks over 2000–10 and Comparisons to
927	Climate Models, <i>Journal of Climate</i> , 26, 333–342, doi:10.1175/JCLI-D-11-00640.1.

928	
929	Goodwin, P. (2021), Probabilistic projections of future warming and climate sensitivity
930	trajectories, Oxford Open Climate Change, 1, 1, kgab007,
931	https://doi.org/10.1093/oxfclm/kgab007
932	
933	Goodwin, P. & Cael, B.B. (2021), Bayesian estimation of Earth's climate sensitivity and transient
934	climate response from observational warming and heat content datasets. Earth System
935	Dynamics, 12, 709–723, doi:10.5194/esd-12-709-2021.
936	
937	Goodwin, P. & Williams, R.G. (2023) On the Arctic Amplification of surface warming in a
938	conceptual climate model, <i>Physica D: Nonlinear Phenomena</i> , doi:10.1016/j.physd.2023.133880
939	
940	Goodwin, P., Williams, R.G., Ceppi, P. and Cael., B.B. (2024 submitted) Spatial Climate Feedback
941	model code [model code] (the model code developed for this study, which will be made
942	permanently available with doi after acceptance of the manuscript)
943	
944	Hartmann, D.L. (1994), Global Physical Climatology, Academic Press, San Diego, USA. ISBN 0-12-
945	328530-5. 411 pp.
946	
947	Hersbach, H., Muñoz Sabater, J., Nicolas, Rozum, I., Simmons, Vamborg, F., A., Bell, B.,
948	Berrisford, P., Biavati, G., Buontempo, C., Horányi, A., J., Peubey, C., Radu, R., Schepers, D., Soci
949	C., Dee, D. & Thépaut, J-N. (2018), Essential climate variables for assessment of climate

950	variability from 1979 to present, Copernicus Climate Change Service (C3S) Data Store (CDS),
951	(Accessed on 31-03-2024) [Dataset] <a href="https://doi.org/10.24381/cds.f17050d7">https://doi.org/10.24381/cds.f17050d7</a>
952	
953	Ingram, W. (2010) A very simple model for the water vapour feedback on climate change. Q. J.
954	R. Meteorol. Soc. 136, 646, 30-40. https://doi.org/10.1002/qj.546.
955	
956	IPCC (2021), Climate Change 2021: The Physical Science Basis. Contribution of Working Group
957	to the Sixth Assessment Report of the Intergovernmental Panel on Climate Change [Masson-
958	Delmotte, V., Zhai P., Pirani, A., Connors, S.L., Péan, C., Berger, S., Caud, N., Chen, Y., Goldfarb,
959	L., Gomis, M.I., Huang, M., Leitzell, K., Lonnoy, E., Matthews, J.B.R., Maycock, T.K., Waterfield,
960	T., Yelekçi, O., Yu, R., and Zhou, B. (eds.)]. Cambridge University Press, Cambridge, United
961	Kingdom and New York, NY, USA, doi: 10.1017/9781009157896.
962	
963	Koll, D.D.B., and Cronin, T.W. (2018) Earth's outgoing longwave radiation linear due to $\rm H_2O$
964	greenhouse effect. Proc. Natl. Acad. Sci. U.S.A. 115 (41) 10293-10298.
965	https://doi.org/10.1073/pnas.1809868115.
966	
967	Loeb, N.G., Doelling, D.R., Wang, H., Su, W., Nguyen, C., Corbett, J.G., Liang, L., Mitrescu, C.,
968	Rose, F.G. and Kato, S. (2018), Clouds and the earth's radiant energy system (CERES) energy
969	balanced and filled (EBAF) top-of-atmosphere (TOA) edition-4.0 data product. Journal of
970	Climate, 31(2), 895-918, doi:10.1175/JCLI-D-17-0208.1.

972	Mateus, P., Mendes, V.B. and Pires, C.A.L. (2022), Global Empirical Models for Tropopause
973	Height Determination, Remote Sensing 14, 4303, doi:10.3390/rs14174303.
974	
975	Mateus, P., Mendes, V.B. and Pires, C.A.L. (2022b), Global Tropopause Models [model code].
976	Accessed via <a href="https://github.com/pjmateus/global tropopause model">https://github.com/pjmateus/global tropopause model</a> (associated with
977	doi:10.3390/rs14174303)
978	
979	NASA/LARC/SD/ASDC. (2022). CERES Energy Balanced and Filled (EBAF) TOA Monthly means
980	data in netCDF Edition4.2 [Dataset]. NASA Langley Atmospheric Science Data Center DAAC.
981	Retrieved from <a href="https://doi.org/10.5067/TERRA-AQUA-NOAA20/CERES/EBAF-TOA">https://doi.org/10.5067/TERRA-AQUA-NOAA20/CERES/EBAF-TOA</a> L3B004.2
982	
983	
984	Payne, R.E. (1972) Albedo of the Sea Surface. Journal of the Atmospheric Sciences, 25, 5, 959-
985	970. doi:10.1175/1520-0469(1972)029<0959:AOTSS>2.0.CO;2
986	
987	Raval, A., Ramanathan, V. (1989) Observational determination of the greenhouse
988	effect. Nature 342, 758–761. <a href="https://doi.org/10.1038/342758a0">https://doi.org/10.1038/342758a0</a>
989	
990	Schmidt, G.A., Ruedy, R., Miller, R.L., and Lacis, A.A. (2010) Attribution of the present-day total
991	greenhouse effect. J. Geophys. Res., 115, D20106, https://doi.org/10.1029/2010JD014287
992	

Sherwood, S. C., Webb, M. J., Annan, J. D., Armour, K. C., Forster, P. M., Hargreaves, J. C., 993 994 Hegerl, G., Klein, S. A., Marvel, K. D., Rohling, E. J., Watanabe, M., Andrews, T., Braconnot, P., Bretherton, C. S., Foster, G. L., Hausfather, Z., von der Heydt, A. S., Knutti, R., Mauritsen, 995 T., Norris, J. R., Proistosescu, C., Rugenstein, M., Schmidt, G. A., Tokarska, K. B. & Zelinka, M. 996 997 D. (2020). An assessment of Earth's climate sensitivity using multiple lines of evidence. Reviews of Geophysics, 58, e2019RG000678. https://doi.org/10.1029/2019RG000678 998 999 1000 Soden, B. J., Held, I.M., Colman, R., Shell, K.M., Kiehl, J. T. & Shields, C. A. (2008), Quantifying 1001 Climate Feedbacks Using Radiative Kernels, Journal of Climate, 21, 3504–3520, doi:10.1175/2007JCLI2110.1. 1002 1003 1004 Stephens, G.L. (1978), Radiation Profiles in Extended Water Clouds. II: Parameterization 1005 Schemes. Journal of Atmospheric Sciences 35, 2123-2132, doi:10.1175/1520-0469(1978)035<2123:RPIEWC>2.0.CO;2. 1006 1007 Taylor, K. E., Crucifix, M., Braconnot, P., Hewitt, C. D., Doutriaux, C., Broccoli, A. J., Mitchell, J. F. 1008 1009 B. and M. J. Webb (2007), Estimating Shortwave Radiative Forcing and Response in Climate 1010 Models, Journal of Climate, 20, 2530-2543, doi:10.1175/JCLI4143.1. 1011 1012 USGS (2011) GMTED2010 global digital elevation model (accessed 18/03/2024) [Dataset]. Available https://temis.nl/data/gmted2010/ 1013

1015	WCRP (2024) Coupled Model Intercomparison Project (Phase 6) [Dataset] (Accessed
1016	08/04/2024) https://esgf-index1.ceda.ac.uk/search/cmip6-ceda/
1017	
1018	Zelinka, M. D., Myers, T. A., McCoy, D. T., Po-Chedley, S., Caldwell, P. M., Ceppi, P., Klein, S. A. &
1019	Taylor, K. E. (2020), Causes of higher climate sensitivity in CMIP6 models, Geophysical Research
1020	Letters, 47, e2019GL085782, doi:10.1029/2019GL085782.

Figure captions:
<b>Figure 1.</b> Spatial variation in total outgoing radiation correlating with surface temperature for the 2003-2023 period, analyzed as annual-mean climatology, with each dot (a) representing a single location with 1 deg by 1 deg horizontal resolution. Surface temperature (b) evaluated from ERA5 (Hersbach et al., 2023) and outgoing radiation (c) from EBAF4.2 (Loeb et al., 2018).
<b>Figure 2:</b> Monthly climatological planetary emissivity for 2003-2023 from observations (left hand column), a reduced physics simplified empirical relation (middle column) and the error in the empirical relation (right hand column). Shown are planetary emissivity in clear sky conditions (top two rows) and all sky conditions (bottom two rows) for the months of January and July.
<b>Figure 3:</b> Annual climatological albedo in all sky and clear sky conditions from observations (left hand column), from the empirically constrained predictions (middle column) and the error in the empirical predictions (right hand column). The rms error in the empirical relation for planetary albedo is 0.037 for clear sky and 0.069 for all sky conditions.
<b>Figure 4.</b> Spatial variation in outgoing radiation, planetary emissivity and albedo for the 2003-2023 period in clear sky conditions, analyzed as annual-mean climatology for 1° by 1° horizontal resolution. (a) Outgoing longwave radiation in clear sky conditions. (b) Outgoing shortwave radiation in clear sky conditions and surface temperature. (d) Outgoing shortwave radiation in clear sky conditions and surface temperature. (e) Planetary emissivity in clear sky conditions and surface temperature. (f) Planetary albedo in clear sky conditions and surface temperature.
<b>Figure 5.</b> Local albedo over land and ocean with surface temperature for the climatological period 2003-2023. (a) The local annual-mean clear sky planetary albedo with surface temperature evaluated over 1° by 1° resolution. (b) The implied global-mean clear sky planetary albedo if the entire planet was covered in the surface-type found at that location, evaluated over 1° by 1° resolution.
<b>Figure 6.</b> The albedo of cloud for directed incident solar radiation (left hand panels) and the cloud emissivity coefficient for outgoing longwave radiation (right hand panels) and the albedo of cloud from monthly mean climatology for 2003-2023.

Figure 7. Surface albedo feedback spatially and as a zonal average in clear sky and all sky 1057 1058 conditions. The spatial surface albedo feedback for the 2003-2023 period for (a) clear sky and 1059 (b) all sky conditions. The zonal mean surface albedo feedback for (c) clear sky and (d) all sky 1060 conditions. Zonal mean feedbacks shown are for infinitesimal perturbation starting from the 2003-2023 climatology (blue), starting from a 2K warmed climate state (red) and starting from a 1061 1062 4K warmed climate state (orange). Zonal mean feedback for finite 4xCO<sub>2</sub> perturbation is shown 1063 for CMIP6 models (grey), evaluated from radiative kernels. 1064 1065 Figure 8. The WVLR feedback spatially and as a zonal average for clear sky and all sky 1066 conditions. The spatial WVLR feedback for the 2003-2023 period for (a) clear sky and (b) all sky 1067 conditions. The zonal mean WVLR feedback for (c) clear sky and (d) all sky conditions. Zonal 1068 mean feedbacks shown are for infinitesimal perturbation starting from the 2003-2023 1069 1070 climatology (blue) and for finite 4xCO<sub>2</sub> perturbation for CMIP6 models (grey), evaluated from 1071 radiative kernels. 1072 Figure 9. Frequency distributions for effective global mean climate feedback, and values for 1073 1074 individual CMIP6 models. Shown are constraints from spatial evidence from this study (blue line), and externally calculated temporal evidence values including for CMIP6 models (gray 1075 crosses: Zelinka et al., 2020), and from a recent review (black dashed line: Sherwood et al., 1076 1077 2020). 1078

# **Table and Table caption:**

1079
1080

Climate feedback	This study, 2003-2023 {median, (66% range) [90% range]}	This study, +2°C warming {median, (66% range) [90% range]}	This study, +4°C warming {median, (66% range) [90% range]}	AR6 {median, (66% range) [90% range]}	Sherwood et al. {median, (66% range) [90% range]}	CMIP6, {mean ± standard deviation}
Planck, λ <sub>Planck</sub> (Wm <sup>-2</sup> K <sup>-1</sup> )	-3.30	-3.38	-3.52	-3.22 (-3.1 to -3.3) [-3.0 to -3.4]	-3.20 (-3.16 to -3.24) [-3.13 to -3.27]	-3.28±0.05
Surface albedo, $\lambda_{albedo}$ (Wm $^{-2}$ K $^{-1}$ )	0.60 (0.53 to 0.66) [0.49 to 0.70]	0.50 (0.45 to 0.55) [0.41 to 0.59]	0.32 (0.28 to 0.35) [0.26 to 0.37]	0.35 (0.25 to 0.45) [0.10 to 0.60]	0.30 (0.15 to 0.45) [0.05 to 0.55]	0.45±0.09
WVLR, $\lambda_{WVLR}$ (Wm <sup>-2</sup> K <sup>-1</sup> )	1.30 (1.20 to 1.40) [1.12 to 1.47]	1.32 <sup>a</sup> (1.21 to 1.42) [1.13 to 1.49]	1.36 <sup>a</sup> (1.24 to 1.48) [1.16 to 1.56]	1.30 (1.2 to 1.4) [1.1 to 1.5]	1.15 (1.0 to 1.3) [0.9 to 1.4]	1.33±0.09
Cloud, λ <sub>Cloud</sub> (Wm <sup>-2</sup> K <sup>-1</sup> )	-	-	-	0.42 (0.12 to 0.72) [-0.10 to 0.94]	0.45 (0.12 to 0.78) [-0.09 to 0.99]	0.42±0.36
Total climate feedback, $\lambda_{total}$ (Wm <sup>-2</sup> K <sup>-1</sup> )	-0.99 <sup>b</sup> (-0.75 to -1.22) [-0.59 to -1.39]	-	-	-1.16 (-0.78 to -1.54) [-0.51 to -1.81]	-1.30 (-0.86 to -1.74) [-0.58 to -2.02]	-1.00±0.34

Table 1: Climate feedback terms and climate sensitivity compared to IPCC Assessment and CMIP models. CMIP6 values taken from Zelinka et al. (2020). <sup>a</sup>Inferred values for a linearized system, without strong constraints for the second derivative of planetary emissivity with respect to surface temperature. <sup>b</sup>Combines Planck, WVLR and albedo feedbacks with Ceppi and Nowack (2021) evaluated range for cloud feedback.

Figure :	1.
----------	----

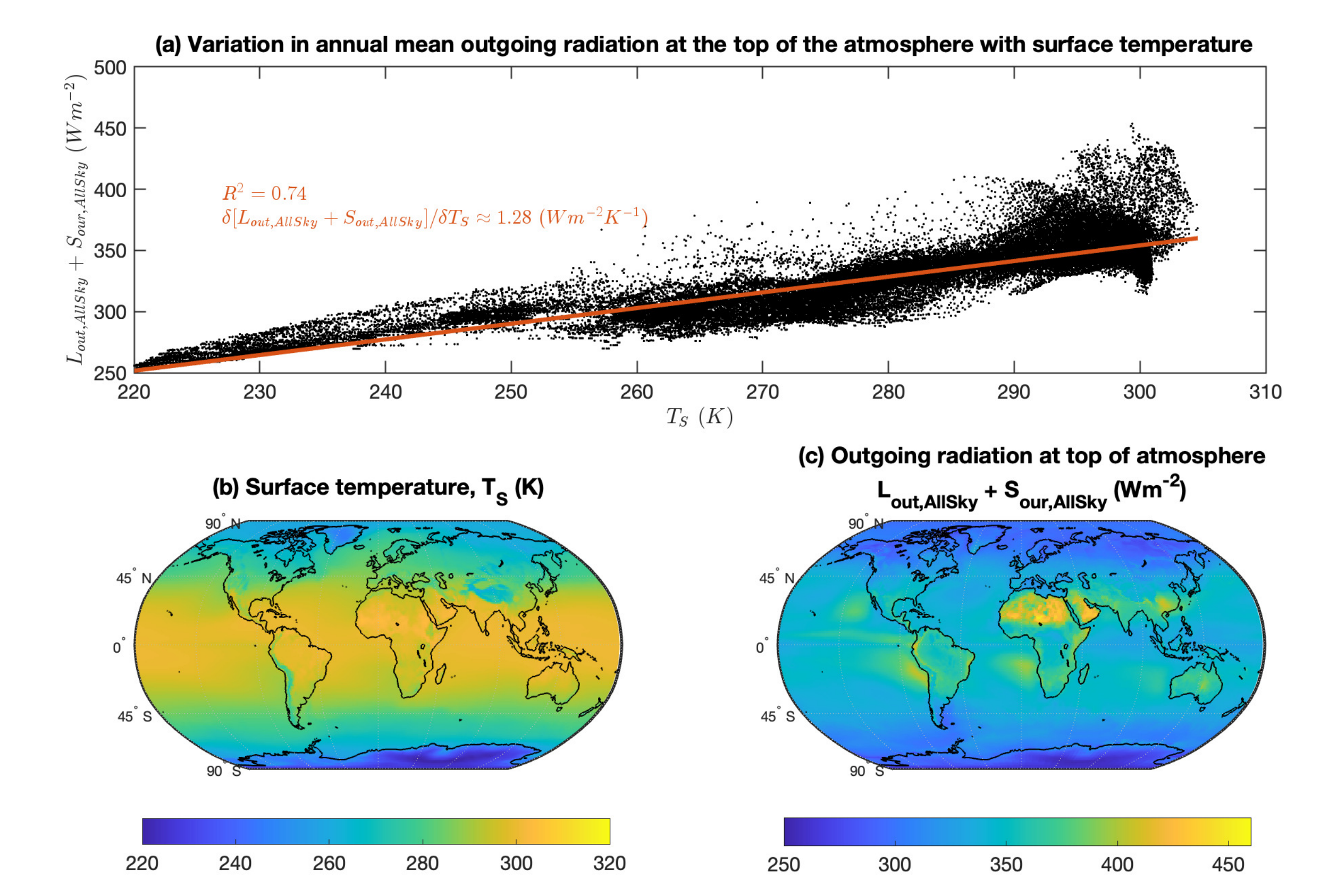


Figure 2	2.
----------	----

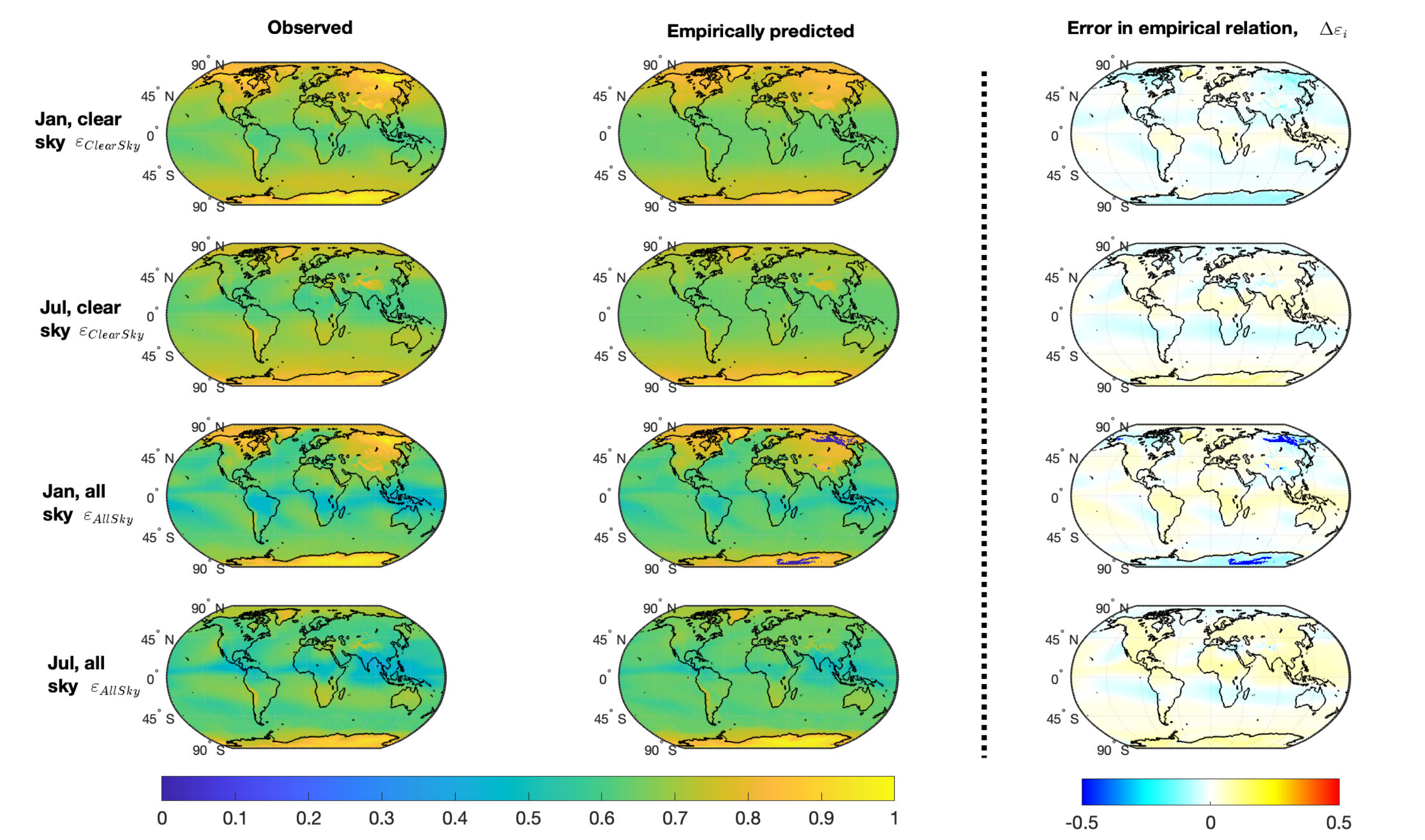


Figure	3.
--------	----

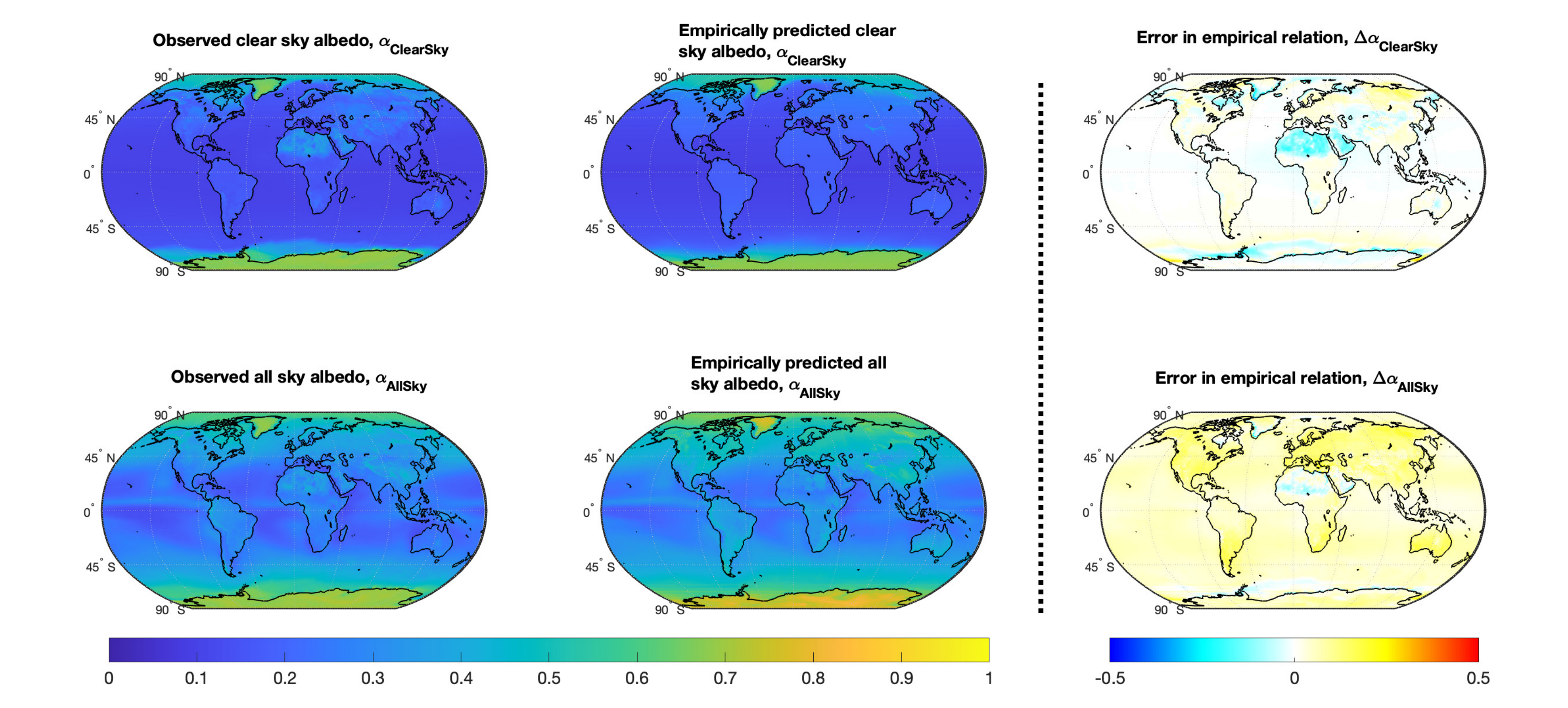


Figure 4.	
-----------	--

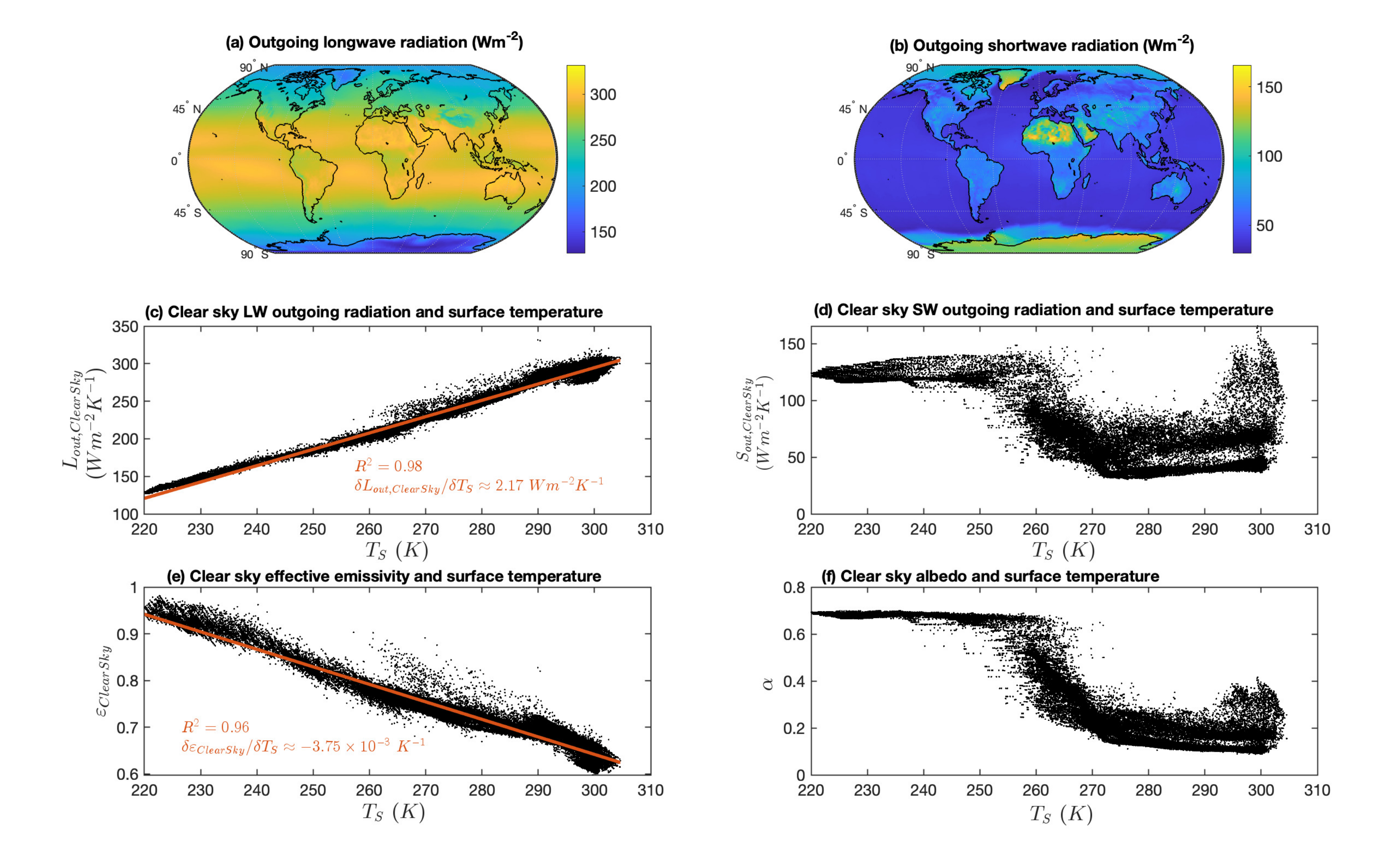
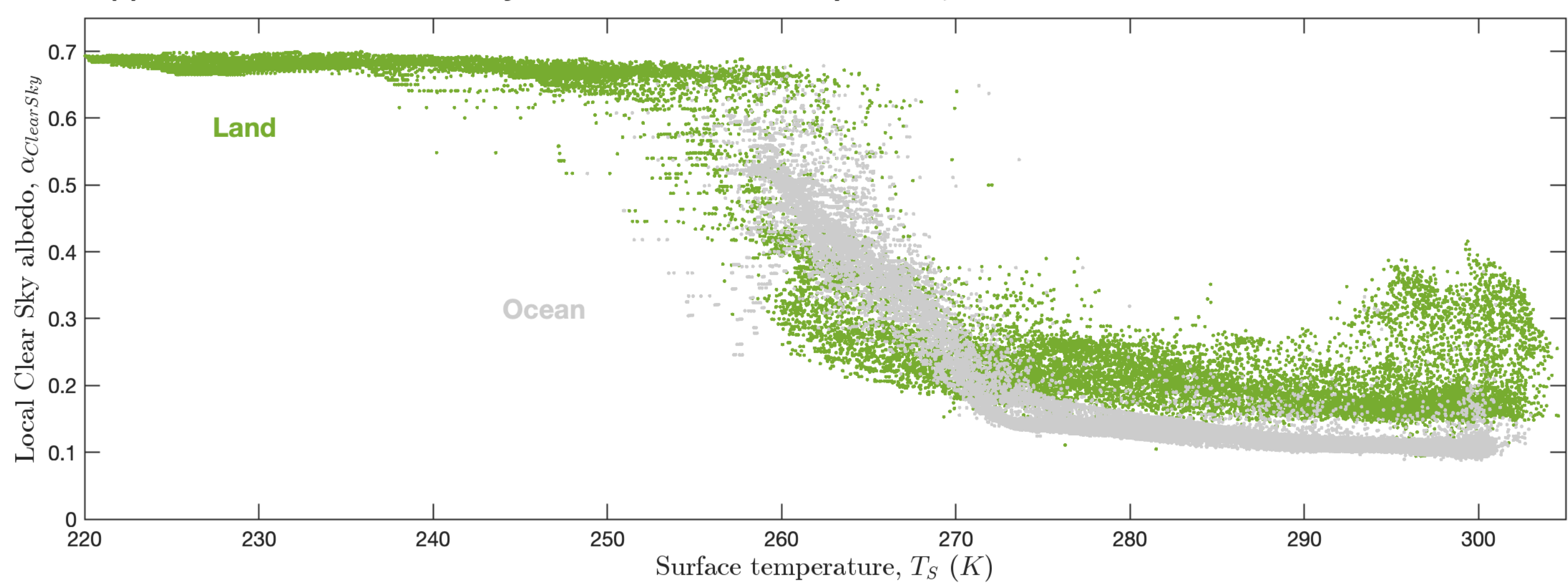


Figure 5.	
-----------	--







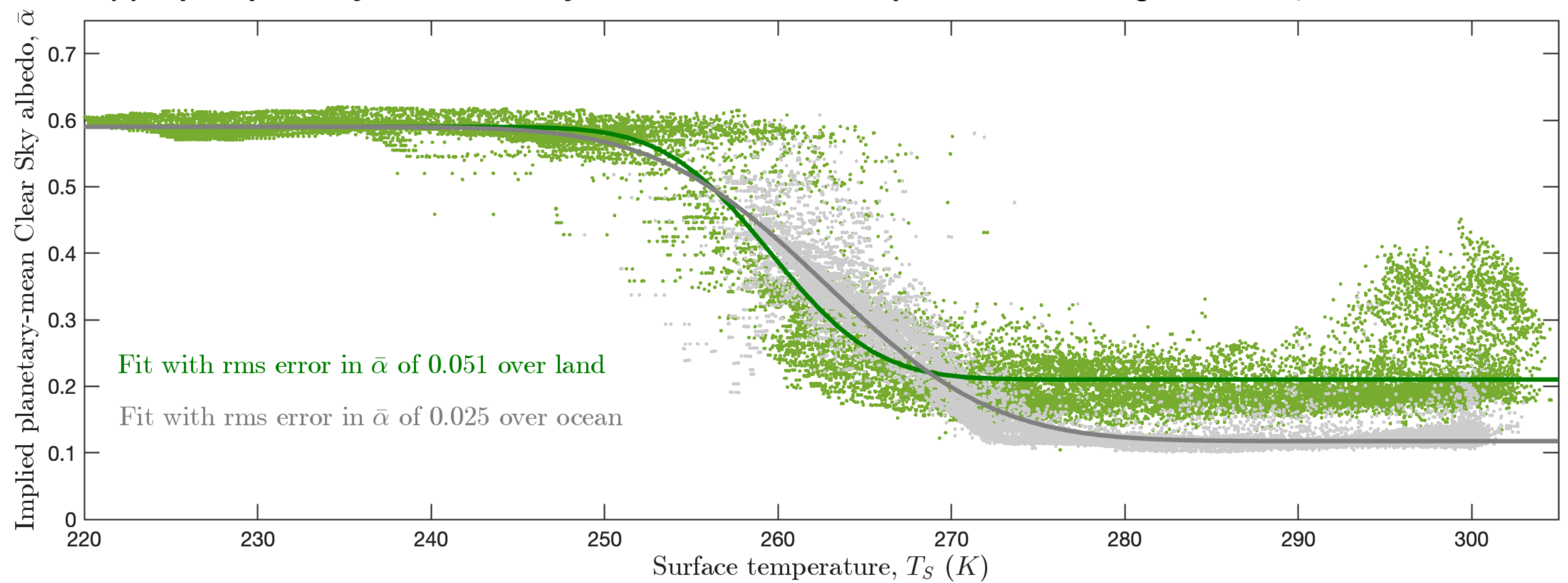


Figure 6	5.
----------	----

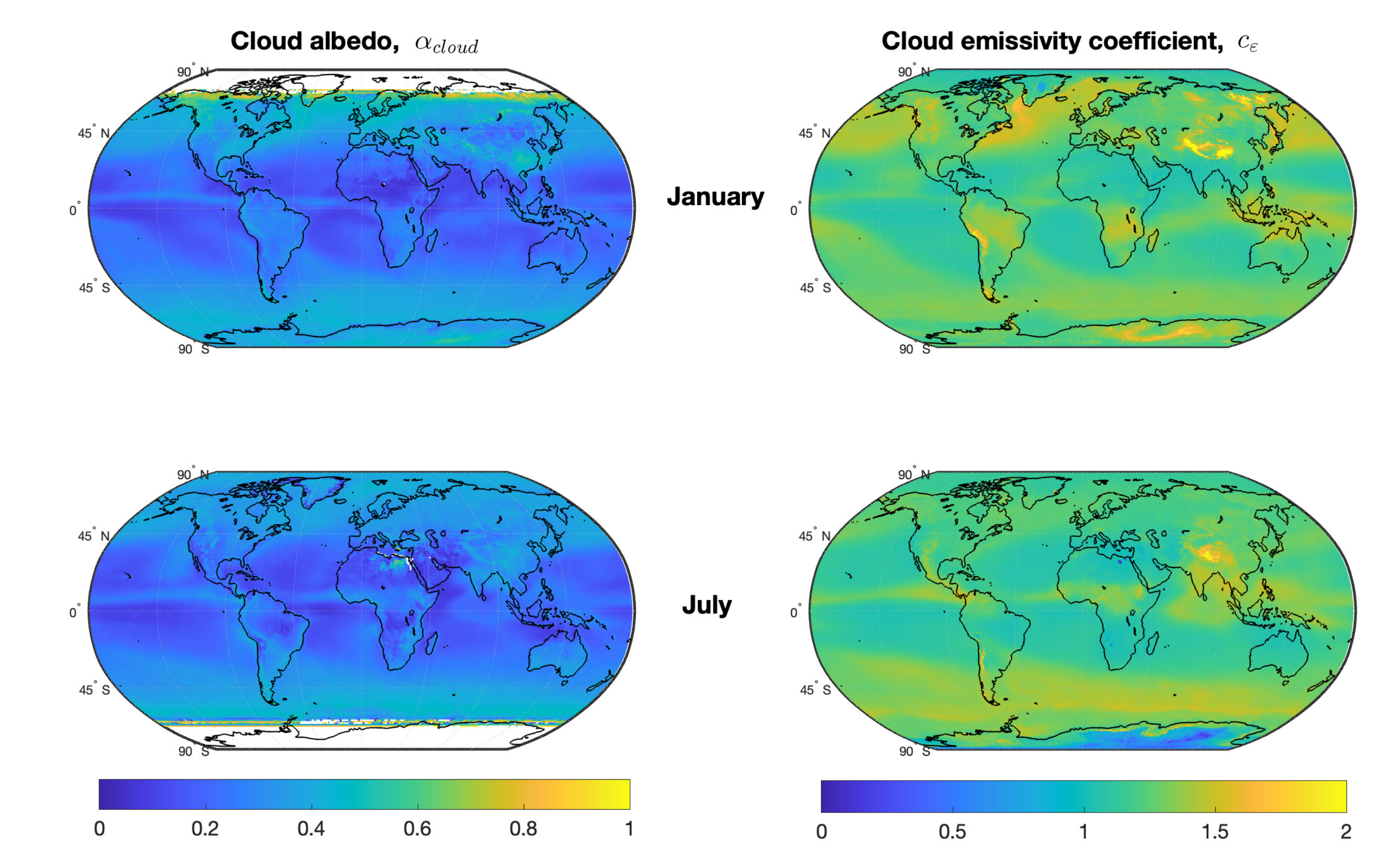


Figure 7.	
-----------	--

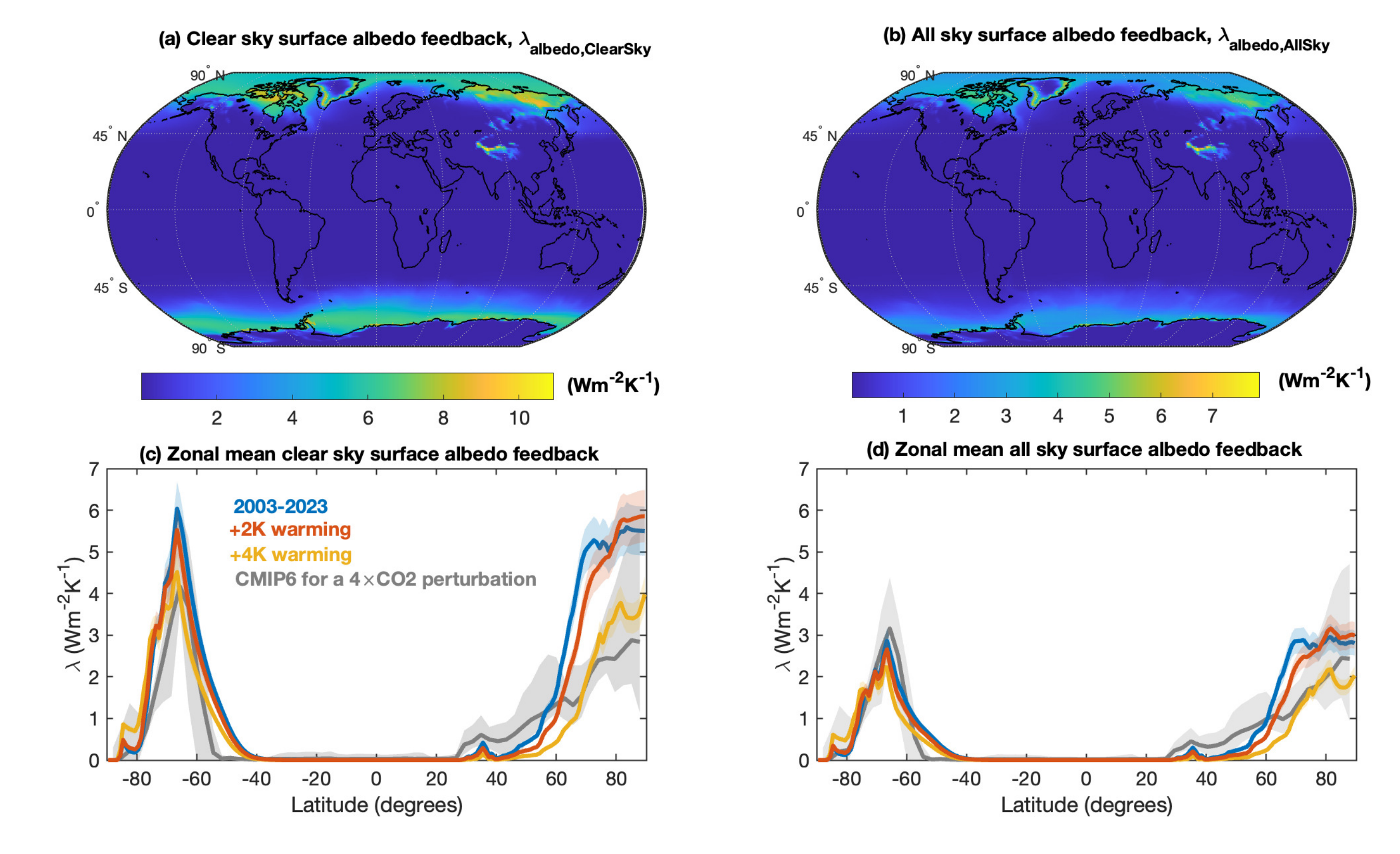


Figure 8.	
-----------	--

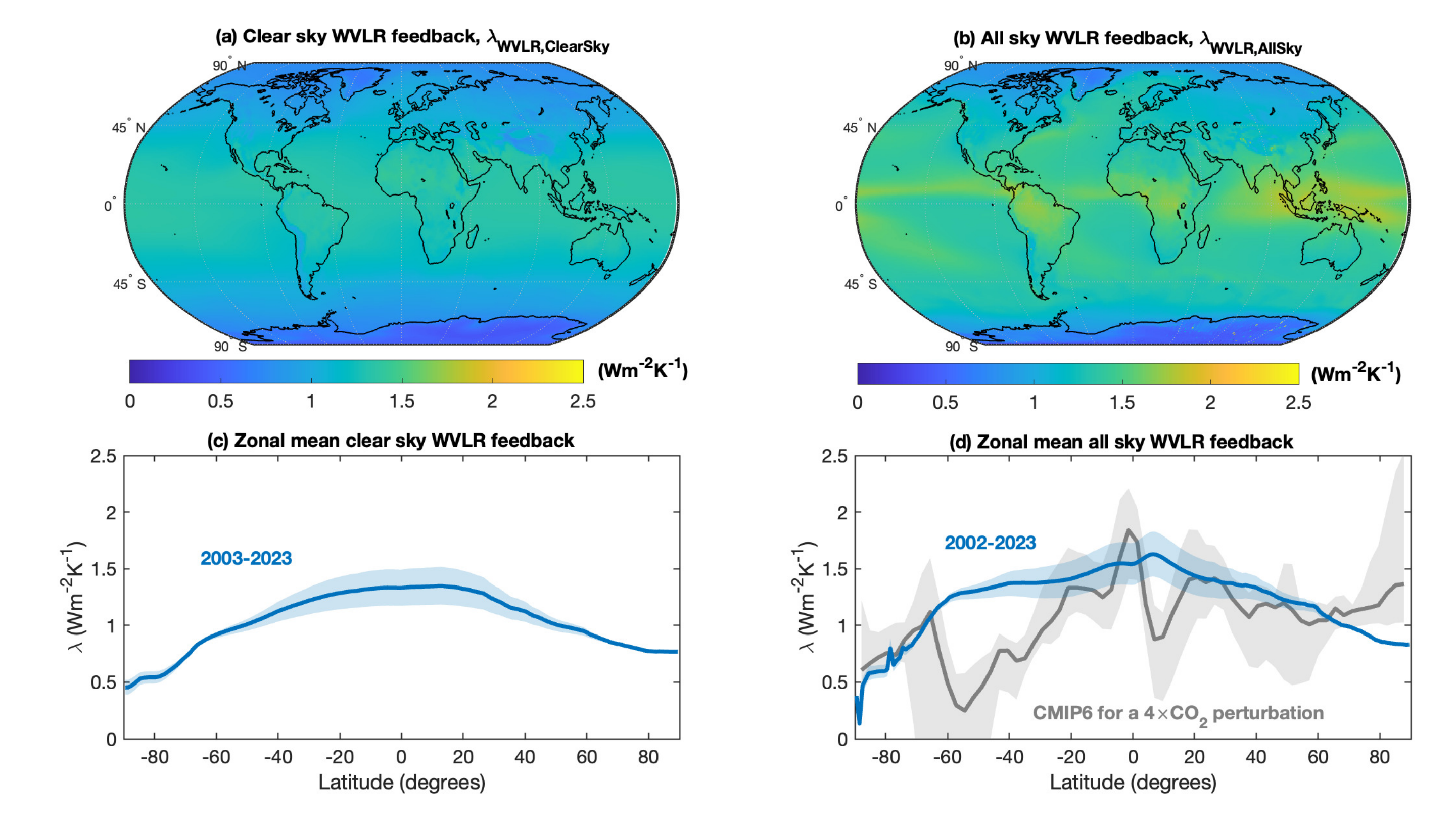


Figure 9.	
-----------	--

